NTNU

Norwegian University of
Science and Technology

Electrical and structural properties of multicrystalline silicon grown from reusable silicon nitride crucibles

Kristoffer Harr Martinsen

Chemical Engineering and Biotechnology
Submission date: August 2016
Supervisor: Eivind Øvrelid, IMTE
Co-supervisor: Martin Bellmann, SINTEF

Norwegian University of Science and Technology
Department of Materials Science and Engineering

Preface

This master thesis is the culmination of my years as a student in the master's program Chemical Engineering and Biotechnology at the Norwegian University of Science and Technology, NTNU, and was conducted at the Department of Materials Science and Engineering. It was written parallel to the international research project Eco-Solar which was funded by the European Union and represented at NTNU through SINTEF, in an ongoing effort to improve quality and commercialization of multi-crystalline solar grade silicon.

Throughout this final, challenging year I have been fortunate enough to receive help and guidance from many. I would like to thank my supervisor Eivind Øvrelid for all advice and input he has given me. I would also like to thank my co-supervisor Martin Bellmann who aided me in formulating the thesis' problem, provided data from the gas chromatography as connected me with other knowledgeable scientists and technicians at SINTEF. Among them I give thanks to Birgitte Karlsen who helped me greatly with numerous equipment and machines (without you I would be lost), and Kai Erik Ekstrøm for valuable input on how to proceed with my measurements and for graciously letting me use his FTIR data. A big thanks goes to Gaute Stokkan for providing me with samples and many useful discussions about the project and how to proceed, even though my visits were sometimes less than opportune.

Another who deserves honorable mention is Dr. Ludovic Jeanniot PhD for his invaluable assistance in continuously motivating and reviewing my thesis.

My greatest gratitude was saved for last and goes to my family – my sister, mom, stepfather and father. Thank you all for being there for me. Thank you all for laughing with me, pushing me forward and helping me surmount this challenge. Especially you, Mom. I do not think I could have done this without your supporting pep talks over the phone.

Kristoffer Harr Martinsen

Trondheim, August 23 2016

Abstract

The solar cell industry has grown considerably and experiences renewed public interest due to technological advances and awareness of human impact on the environment.

However, the industry faces several challenges that must be overcome, such as reduction in ingot production costs without affecting solar cell performance. One promising prospect is by replacing the standardized silica crucibles used in directional solidification, as they can only be used once due to breaking after each ingot solidification and are also known to contaminate silicon ingots with oxygen through diffusion.

In this work, oxidized nitride bonded silicon nitride (NBSN) crucibles were investigated as a potential replacement for silica crucibles. The work includes solidification in both NBSN and standardized silica crucibles. NBSN crucible was reused for comparative study against the standard. Two ingots from each crucible type were investigated with respect to the following:

- Carrier lifetime mapping by µPCD.
- Resistivity mapping by eddy currents. Resistivity as a function of ingot height was also investigated with FPP.
- O_i and C_s concentrations by FTIR.
- Furnace gas composition by *in situ* gas chromatography.

In addition, the contact angle on both uncoated and coated NBSN substrates was measured by the sessile drop method.

Coated NBSN substrate displayed satisfactory non-wetting contact with liquid silicon, but the results from µPCD lifetime mapping imply that NBSN crucibles impose considerable thermal strain in the ingot, as verified by unfavorable grain orientations and high dislocation concentration in the ingot center. These trends and consequent loss in carrier lifetime increased after NBSN crucible reuse, to a maximum of 6 µs. Both ingots solidified in NBSN crucible displayed considerably increased O_i and C_s contamination relative to the references. O_i concentration decreased to below 10 ppma levels after reuse, but C_s remained relatively unaffected and above 7 ppma. Overall resistivity converged to $1{,}5 \pm \pm 0.5$ Ωcm, which was deemed acceptable.

Increased O_i and C_s contamination was attributed to deoxidization of NBSN crucible and increased CO gas diffusion into the silicon melt, respectively.

Keywords:

Multi-crystalline, silicon, p-type. solar cells, NBSN crucible, silica crucible, thermal strain, lifetime, resistivity, impurity, interstitial oxygen, substitutional carbon.

Sammendrag

Solcelleindustrien har vokst betydelig merket fornyet interesse på grunn av teknologiske framskritt, samt bedre forståelse over menneskets innflytelse på miljøet.

Likevel er det fortsatt flere utfordringer som må overvinnes, slik som reduksjonen av produksjonskostnader for silisiumblokker uten å påvirke ytelsen. Et lovende prospekt er å erstatte standarddigelen av silika som brukes i direksjonell størkning, ettersom den kan kun brukes én gang på grunn av oppsprekking etter at blokken er størknet. Dessuten er det kjent at silika forpester silisiumblokkene med oksygen via diffusjon.

I denne hovedoppgaven ble oksiderte digeler av nitridbundet silisiumnitrid (NBSN) undersøkt som en potensiell erstatning. Arbeidet inkluderer størkning i både NBSN og standarddigel av silika. NBSN-digelen ble gjenbrukt for komparativ studie mot silika. To blokker fra hver digeltype ble undersøkt med henhold til følgende:

- Levetid via skanning med µPCD.
- Skanning av resistivitet med eddy-strøm. Resistivitet som funksjon av blokkhøyden ble dessuten undersøkt med FPP.
- Konsentrasjoner av O_i og C_s med FTIR.
- Smelteovnens gasskomposisjon ble undersøkt med *in situ* gasskromatorafi.

I tillegg ble kontaktvinkelen på både belagt og ubelagt NBSN-substrater undersøkt med fastsettende dråpemetode.

Belagt NBSN-substrat viste tilfredsstillende, ikke-fuktende kontakt med flytende silisium, men resultatet fra levetidsskann med µPCD antyder at NBSN-digeler forårsaker betydelig termisk stress i blokken, hvilket var observert som ugunstig kornorientering samt høy dislokasjonstetthet i blokkens sentrum. Disse trendene, samt reduksjon av elektrisk levetid til 6 µs, økte etter gjenbruk av NBSN-digel. Begge blokkene som størknet i NBSN-digel viste betydelig økt forurensning av O_i og C_s relativt til referansedigelene. O_i-forurensning redusertes til under 10 ppma etter gjenbruk, mens konsentrasjonen av C_s fremsto som relativt upåvirket og over 7 ppma.

For alle blokkene konvergerte resistiviteten gitt av blokkhøyde mot $1{,}5 \pm \pm 0.5$ Ωcm, hvilket ble ansett for å være akseptabelt. Økt forurensning av O_i og C_s ble henholdsvis tilskrevet deoksideringen av NBSN-digelen og økt diffusjon av CO-gass inn i smelten.

Nøkkelord:

Multikrystallinsk, silisium, p-type. solceller, NBSN-digel, silikadigel, termisk stress, levetid, resistivitet, urenhet, interstitielt oksygen, substitusjonelt karbon.

List of symbols

C_0	Initial impurity concentration
C_S	Impurity concentration in solid
D_l	Diffusivity in liquid
E_{F_n}	Fermi energy level of electron in trap state
E_{F_p}	Fermi energy level of hole in trap state
E_F	Fermi energy
E_{Ph}	Photon energy
E_g	Bandgap energy
E_t	Impurity/trap energy level
P_{O_2}	Partial pressure of oxygen
$U_{Aug,n}$	Auger recombination rate of electrons
$U_{Aug,p}$	Auger recombination rate of holes
U_{Aug}	Total Auger recombination rate
U_{SHR}	Trap-assisted recombination rate
$U_{n,rad}$	Radiative recombination rate of electrons
$U_{p,rad}$	Radiative recombination rate of holes
a_o	Interatomic distance at equilibrium
f_M	Fraction of mass
f_S	Fraction of solidification
k_0	Segregation coefficient at equilibrium
k_{eff}	Effective segregation coefficient
n_{p_o}	Minority electron concentration before recombination
n_i	Intrinsic concentration of holes/electrons
n_p	Minority electron concentration after recombination
n_t	Concentration of electrons in trap state
p_{n_o}	Minority hole concentration before recombination
p_n	Minority hole concentration after recombination
p_t	Concentration of holes in trap state
Γ_n	Auger coefficient for electrons
Γ_p	Auger coefficient for holes
γ_{LG}	Interfacial energy between a liquid and gas phase
γ_{SG}	Interfacial energy between a solid and gas phase
γ_{SL}	Interfacial energy between a solid and liquid phase
θ_0	Initial contact angle
θ_C	Contact angle
μ_n	Mobility of electrons
μ_p	Mobility of holes

$\tau_{n,SHR}$	Lifetime of electrons prior capture by trap states
τ_n	Lifetime of electrons
$\tau_{p,SHR}$	Lifetime of holes prior to capture by trap states
τ_p	Lifetime of holes
h	Planck's constant
k	Boltzmann's constant
T	Temperature
κ	Thermal conductivity coefficient
λ	Wavelength
A	Absorbance
E	Energy
I	Current
N	Number of atoms
S	Solubility
V	Voltage
a	Absorptivity
b	Thickness
c	Speed of light in vacuum
c	Concentration (Beer's Law)
e, q	Elementary particle charge
f	Frequency
k	Phonon momentum
n	Concentration of electrons
p	Concentration of holes
r	Interatomic distance
δ	Boundary layer thickness
ν	Ingot growth rate
π	Pi constant
ρ	Resistivity
σ	Conductivity

List of figures

List of tables

List of abbreviations

ARC	Anti-reflective coating
CB	Conduction band
CID	Carrier induced degradation
C-SI	Crystalline silicon
DS	Directional solidification
FPP	Four-point probe
FTIR	Fourier transform infrared spectrometry
GC	Gas chromatography
IR	Infrared
LID	Light induced degradation
MC-SI	Multi-crystalline silicon
MO	Molecular orbital
NBSN	Nitride bonded silicon nitride
PCD	Photoconductive decay
PEP	Pauli exclusion principle
PPMA	Parts per million atoms
RF	Radio frequency
SHR	Shockley-Hall-Read
SINTEF	Stiftelsen for industriell og teknisk forskning English: The Foundation for Scientific and Industrial Research
SOG	Solar grade
VB	Valence band
VHL	Vertical heat leak

Table of Contents

1. Introduction

In recent years there has been a monumental increase in research and production of so-called green technologies. This change towards a more sustainable and environmentally friendly society has been called "the green revolution" and is attributed to the increased awareness of human influence on the climate and our ecosystems. While coal, natural gas and nuclear plants remains the primary source for power generation in most countries, there is a consensus that a paradigm shift has occurred and more sustainable technologies will be the subject of considerable growth in the years to come. Thus the solar cell industry has seen steady growth over a few decades as it strives to no longer remain a niche technology, but rather a valid alternative to more traditional power industries.

Currently, solar cell panels made of silicon has the largest market share of solar technology. This is largely due to the material's abundance in the earth's crust. In addition, the production and principles behind silicon is well documented. Multi-crystalline silicon (mc-Si) solar cells constitute about 60% of the market share and, contrary to its crystalline counterpart (c-Si), it benefits from reduced manufacture expenses albeit at the cost of photon conversion efficiency[1], e.g. its capacity to generate electric power from sunlight. Ever since the commercialization of silicon solar cells there has been a profound scientific interest in improving photon absorbance, majority carrier lifetime and reduction of recombination rates. Therefore the highest reported photon conversion efficiency in 2015 for mc-Si and c-Si were 18,5% and 22,9%, respectively[2].

During the production phase of silicon ingots, a number of problematic factors diminish cell performance and add to costs in the product value chain. Two major problems that frequently occur during the directional solidification of silicon are discriminated: 1) inclusion of impurity elements and 2) presence of defects and dislocations:

1) Inclusion of impurities

Inclusion of impurities reduces the total power generation substantially. Such elements are typically transition metal impurities like iron (Fe) and aluminium (Al) that create complex-pairs with other, benign impurities (dopants) such as boron or phosphorous. In addition to metallic impurities there is also a presence of interstitial oxygen (O_i) and substitutional carbon (C_s) that have a negative effect on carrier lifetime. Boron-doped crystalline silicon is particularly sensitive to oxygen

Commented [J1]: e.g. example
i.e. definition (your case here)

Formatted: English (United States)

Formatted: Font: Bold, Italic, English (United States)

Formatted: Font: Bold, Italic, English (United Kingdom)

Formatted: Normal, Indent: First line: 1 cm, No bullets or numbering

Formatted: Indent: First line: 0 cm

concentration as boron combines with oxygen under illumination, thus annihilating the dopant's charge carrier generation[3]. This light-induced degradation (LID) in boron doped silicon has also been observed in mc-Si, albeit to less detriment than for crystalline silicon. Inclusions of nitrogen (N) in the form of silica nitrides is also believed to create shunts in the solar cell, thus lowering performance.

2) Defects and dislocations

Formatted: Indent: Left: 1 cm, Right: 1 cm, No bullets or numbering

Formatted: Indent: First line: 0 cm

Defects are typically vacancies, inclusions, rearrangements and substitutions occurring in the crystal structure and act as recombination sites for charge carriers. Dislocations in the form of cracks or shifts in a crystal structure also act as recombination sites where electrons are lost, and appear to be easily decorated by impurities. These problems are invariably present in multi-crystalline silicon and are the primary source of its lower efficiency compared to c-Si. Considerable efforts have been made by the research community to reduce their influence and presence during vertical Bridgman growth.

In an effort to push multi-crystalline solar cell technologies into the next generation, the European Union has launched an international research project named Eco-Solar in which nitride bonded silica nitride (NBSN) crucibles for silicon ingot growth constitute one of the key areas of interest. NBSN crucibles ~~for ingot growth~~ aim to remedy some of these and other issues that are commonly caused by conventional silica crucibles. Silica crucibles, although affordable, suffer from a high concentration of oxygen that inevitably diffuse into the silicon melt during the DS process at high temperatures. Due to long holding times at elevated temperatures, oxygen diffusion from silica crucibles becomes a major detriment to carrier lifetime. Also, silica crucibles undergo thermal expansion during heating and causes mechanical strain on the vertical solid interface of the growing silicon ingot. This affects the local concentration of defects, dislocations and grain orientations and ultimately also causes micro-fractures in the silica crucible, thereby limiting it to single use for silicon ingot solidification. Lastly, because silicon wets silica, it is required to coat the crucible with a silicon nitride slurry so that they remain separable after the DS process. On the other hand, NBSN crucibles ~~, on the other hand,~~ have a much lower thermal expansion than silica, contains no appreciable oxygen compounds and is naturally non-wetting in contact with silicon melts. These features make NBSN crucibles a desirable choice for next generation multi-crystalline solar grade silicon and makes multiple re-use of the same crucible feasible, which would ameliorate its value chain considerably by reducing crucible costs with up to 30%.

Research on NBSN crucible type and its properties has been commissioned to the research organization SINTEF, to which this master thesis is closely tied. The aim of this thesis is to investigate the electric properties of multi-crystalline silicon ingots produced through vertical Bridgman growth by directional solidification (DS), in which a silicon feedstock is melted down and vertically solidified at identical rates in both NBSN crucibles and reference crucibles of fused silica. In order to characterize the effect of which NBSN crucibles have on the ingot during solidification, the electrical properties of silicon solidified in both crucible types were analyzed. Transient resistivity and lifetime maps were constructed by microwave photoconductive decay (μPCD) raster scans, while the impurity content in the form of oxygen and carbon is measured by Fourier transform infrared spectroscopy (FTIR). Resistivity is also measured by four-point probes (FPP). In order to attain a better understanding of impurity distribution in the melt, a gas chromatography system was also incorporated into the Crystalox furnace to measure partial pressures of contaminant gases. The aim of this thesis is to investigate the electric properties of multi-crystalline silicon ingots produced through vertical Bridgman growth by directional solidification (DS), in which a silicon feedstock is melted down and vertically solidified at identical rates in both NBSN crucibles and reference crucibles of fused silica.

Commented [J2]: to? or by?

2. Fundamental principles

This chapter covers two fundamental principles.

Formatted: Space Before: 0 pt, After: 6 pt

The solar cell in-depth structure is first described in order to identify the role of impurity, dislocations and defects on cell performance and/or crucible alteration.~~presentsliterature employed in the thesis, which covers fundamental principles of~~ The energy band theory, defining the different type of materials, the design of semiconductor properties and a description of how ~~semiconductors~~ they are affected by impurities, dislocations and grain boundaries, will be explained.

The second principle relates to the theory behind directional solidification and its parameters. This includes~~is also explained.~~ ingot growth, choice of crucible material, impurity segregation and their origin. The effect of gas flows, crystal microstructure and melt convection is also detailed.

2.1. Principles of a solar cell

2.1.1 Energy band theory

Energy band theory is the foundation to our understanding of electrical properties in materials. Quantum theory states that electrons in an atom are energetically restricted to discrete quantum states, meaning that transitions between energy states are limited by specific energy quanta. Another condition that applies is the Pauli Exclusion Principle (PEP)[4] which states that every quantum state can be occupied by up to two fermions, (e.g. electrons), given that they both have mutually opposite spins, thus causing the net spin state to be 0.

As a quantum particle, an electro has the properties of both a particle and a wave and can therefore form new quantum states with other electrons through wave interference. When elements form bonds, one electron with different spin from each atom interact with one another while adhering to the Pauli exclusion principle. This creation of new energy states to form molecules is called the molecular orbital theory and is illustrated in figure 2.1 using a simple molecule F_2 as an example. Similar atomic quantum energy states combine to form new molecular energy states, which is the basis for molecular orbital (MO) theory. This continues until every atomic electron constitutes a molecular orbital, paired if possible. Lower energy levels are called bonding orbitals[4] and are molecular wave functions that interfere constructively, thus contributing to forming a stable molecule because the total energy in the system is reduced. On the other hand, higher energy orbitals in an energy level are called antibonding and appear after destructive interference between orbitals, thus forcing atomic nuclei to separate.

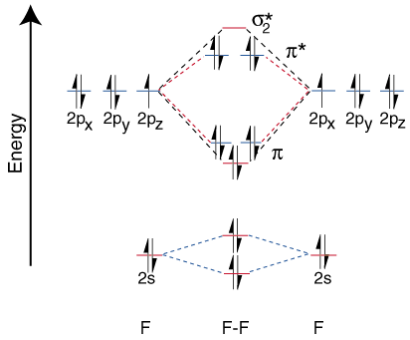

Figure 2.1: MO-diagram of difluoride. Covalent bonding orbitals are formed by lower energy "bonding" states as opposed to higher energy "antibonding" quantum states. (Source: Sparksnotes.com)

Although the example in figure 2.1 used the element fluorine, all elements can form covalent bonds in an analogous manner. As the number of bonding atoms increases to form a

crystal lattice and hence a solid material, the energy separation between bonding and antibonding energy states will approach zero. On the other hand, separation between orbitals like 2s and 2p increases. Eventually the quantum states become so abundant and dense that they create a superposition between orbitals of similar energies and states, thus forming quasi-continuous bands. The degree of energy separation between bands has a considerable influence over the solid's conductive properties.

The lowest energy band, called s-band, is a linear combination of spherical s-orbitals which constitutes the probability space in which an electron can reside at a certain energy. In a quasi-continuous state, the s-orbitals are mutually interlocked with one another and form a network of orbitals. An accurate visualization would be a matrix of marbles which forms a superstructure. Conversely, the dumbbell-shaped p-orbitals of the elements have a lower order of symmetry and therefore energetically unfavorable compared to s-orbitals. Their quasi-continuous state is a higher energy band called the p-band, which is also a superstructure of interlocking p-orbitals. Usually, the s-band and p-band has a large energy separation between them, ensuring that charge carriers are confined to the lowest energy state, the s-band, by a bandgap energy E_g. It is important to that for a pure solid this bandgap contains no energy states in which electrons can be bound and is therefore "forbidden" to electrons. This band energy is a function of interatomic separation, shown in figure 2.2.

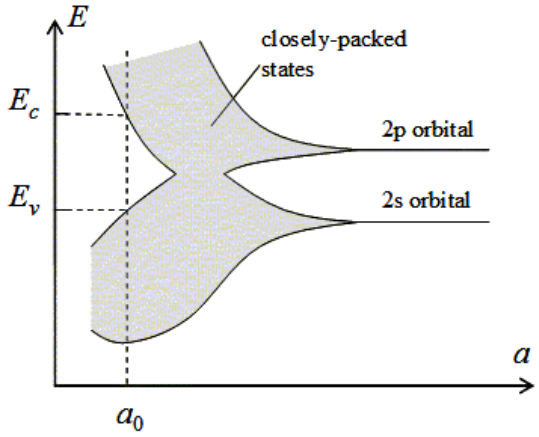

Figure 2.2: Energy bands in a solid as a function of atomic separation, r. At equilibrium the atomic separation is a_o.

The band energy, E_g, is usually only in the order of a few electron volts (eV), a measure which is defined as the potential change of one electron with elementary charge $e \approx 1{,}602 *$

$10^{-19}C$ when it passes a 1 V electric field. However, the bandgap can vary significantly depending on the element composition of the material. The lowest energy band for the material is always filled and called valence band (VB), whereas the empty or partially filled energy band is called conduction band (CB). In order for a material to be conducting, charge carriers like electrons must be able to transition readily between empty quantum states when experiencing an electric field. As the name suggest, the CB energy band is therefore conducting in the sense that it contains many empty quantum states that electrons can transition between. This is shown in figure 2.2 where CB is completely empty at equilibrium atomic separation, a_o.

2.1.2 Bandgap and excitation of electrons

Pure solids can be classified with respect to energy band theory[5] because it largely defines their electrical properties. If all the energy states in the VB are occupied, the band is "filled" pairwise by electrons according to the PEP and does not conduct electrons. Another scenario is when the VB is only partially filled or overlapping CB, resulting in readily available energy states for electrons. According to energy band theory, solids can be classified into three groups:

- Metals
- Insulators
- Semiconductors

Metals are highly conductive materials and can be visualized as a dense matrix of atoms suspended in a sea of electrons. In a metal, electrons are not bound to single atoms and can thus move readily through the solid. In other words, they are delocalized in the solid and can transition between energy states effortlessly. Depending on the type of metal, the high conductivity and delocalized electrons is explained by either a partially filled VB or that VB and CB are overlapping. Regardless of the case, this means that electrons in metals can easily transition between energy states. However, because atomic nuclei have positive charges they repel the negatively charged electrons. This means that conductivity will decrease with temperature as atoms increasingly interfere with electron movement.

Insulators are the exact opposite of metals. Their valence electrons are tightly bound to atoms in covalent chemical bonds due to their crystal structure. Thus they only conduct electricity by breaking these bonds, which requires a considerable amount of energy. Consequently, their VB is completely filled and their CB is empty at room temperature because

a band energy E_g is required to break bonds. Compared with metals, their electrical conductivity is therefore inhibited because no empty energy states are readily available. Unlike metals, their conductivity rises with temperature as more and more bonds obtain enough energy to break. Materials like these are called insulators due to their ability to insulate against electric currents.

Semiconductors have conductive properties that are intermediate to metals and insulators. Their chemical bonds are also covalent in nature but require much less energy to break compared to an insulator. Although their VB is completely filled like for insulators, their E_g is so low that the conductivity increases considerably with temperature due to thermal energy transfer to their binding electrons. Figure 2.3 shows the bandgaps for metals, semiconductors and insulators.

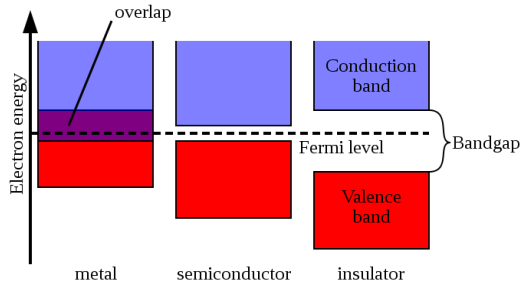

Figure 2.3: Energy band diagram of metals, semiconductors and insulators. The valence band is filled and conductivity for each material is determined by the availability of empty energy states. Conductivity decreases with bandgap separation.

The figure shows that semiconductors, for example silicon, possess electrical properties intermediate to that of metals and insulators. This fact makes them viable for use in electric devices because several factors like bandgap, temperature and the presence of impurity atoms will affect conductivity. Consequently, semiconductors be designed for a multitude of functions such as switches, detectors and diodes.

A special property of semiconductors, such as silicon, is that their electron density of states and conductivity improves according to the Fermi-Dirac distribution[5]:

$$f(E) = \frac{1}{e^{\frac{(E-E_F)}{kT}} + 1} \qquad (2.1)$$

Where E_F is the Fermi energy level, defined as the maximal chemical potential of electrons in a semiconductor at a temperature T of 0 Kelvin (K), and k is the Boltzmann constant. The Fermi-Dirac distribution states the possibility for an electron to occupy an energy

state E at a given temperature. When the temperature increases, the probability for an electron to exist at state E above the Fermi level also increases, as detailed in figure 2.5. Consequently, the probability of unoccupied states existing below the Fermi level also increases.

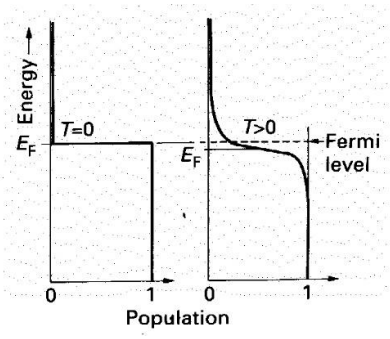

Figure 2.4: Population of energy states as a function of temperature. The population is shifted to energy levels higher than E_F above absolute zero temperature.

In a pure semiconductor the Fermi level is positioned in the middle of the bandgap, so that $E_F = \frac{1}{2}E_g$. As detailed in a later section, alteration of the Fermi level is closely linked to designing electric properties in a semiconductor. This concept is the foundation to modern transistor technology as we know it.

In order for an electron to jump between energy bands, or rather become "excited", an influx energy E is required. This energy can be supplied either as vibrational energy in the form of phonons, electric fields or radiation in the form of photons. For example, whenever thermal excitation occurs in a semiconductor, it leaves behind empty energy states in VB as shown in figure 2.5. The required energy quanta are expressed in terms of electron volts (eV) .

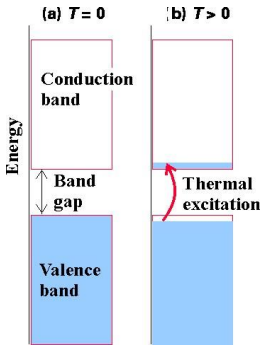

Figure 2.5: Thermal excitation of electrons from valence band to conduction band at T>0 K. As the temperature increases, the extent of thermal excitation will increase.

As the energy is transferred to an electron in CB, the electron becomes excited out of its band and is delocalized. At this point one out of two possibilities will occur to the electron.

If the influx energy was $E \geq E_g$, the electron is successfully excited to the CB and contributes to the conductivity, at least momentarily. The excess energy dissipates as thermal energy released to the crystal lattice in a process called thermalizing, and the void left in VB, called a "hole", will count as a positive charge carrier. Together, the paired and simultaneous creation of hole and electron charge carriers is defined as an exciton, which is a theoretical particle formalized in semiconductor physics.

If $E < E_g$, the electron will be excited but quickly relax back to its initial state and release the wasted energy as phonons (e.g. vibrational energy in the crystal lattice. The energy dissipates quickly as it propagates through the crystal whether phonons are created due to insufficient excitation energy or as excess energy after a successful excitation. There is also a possibility that the excited electron may revert back to VB from CB through various mechanisms and release an energy quantum $E = E_g$ in the process. This is process is called recombination and is detrimental to solar cell photon conversion efficiency.

Compared to metals and insulators, semiconductors are unique in the sense that some of them have an E_g is low enough to allow excitation of electrons from VB to CB by visible light, more precisely photons, thus requiring only a few eV. This unique property makes them viable for photovoltaic applications and power generation. Fortunately, visible light consists of photons of wavelengths (λ) between 400 and 700 nanometers. This constitutes the majority of our sun's electromagnetic radiation and covers many values of E_g for semiconductors. The energy of incident photons, E_{Ph}, is given by the equation

$$E_{Ph} = \frac{hc}{\lambda} = hf \qquad (2.2)$$

Where $h \approx 6.626 \times 10^{-34}\, m^2 kg/s$ is the Planck constant, $c = 3 * 10^8\, m/s$ is the speed of light and f is the photon wave frequency. Solar cells based on silicon therefore absorb photons with energy characteristic to its bandgap $E_g = 1{,}1\ eV$.

2.1.3 Direct and indirect bandgap in semiconductors

The illustration of bandgaps in figure 2.3 is a simplification in the case of semiconductors, because it does not depict whether the bandgap is direct or indirect, which is an intrinsic property that all semiconductors possess. The electrons in a direct bandgap semiconductor, such as GaAs, can be excited to CB largely unaffected by crystal lattice vibrations and is often depicted like figure 2.3 or figure 2.5. However, electrons in indirect bandgap semiconductors like silicon require a change in crystal lattice phonon momentum k to undergo excitation to the lowest available energy level in CB. A phonon is a quantified wave packet of vibrational energy in a crystal which occurs upon kinetic force or heat transfer. For example, if the crystal is heated at one pinpoint location, the energy will spread out from the epicenter as waves of atomic vibrations.

As previously mentioned, the lowest bandgap transition in indirect semiconductors can only be reached by an excited electron if its momentum changes by absorption of a phonon so that $\Delta k \neq 0$. However, an excitation may also occur without a phonon component, but this necessitates a much higher excitation energy and is usually impractical for photovoltaic applications. Although an indirect semiconductor, silicon is the exception among indirect semiconductors due to its direct bandgap being able to absorb visible light. However, direct excitation in most other indirect semiconductors causes the electron to occupy a highly energetic and unstable state. Shortly thereafter, it will relax to a lower energy state by releasing its excess energy in the form of a phonon and photon. This manner of relaxation is one of the main contributors to overheating in silicon solar cells.

Direct bandgap semiconductors, on the other hand, do not need a phonon component to transition to and from the lowest energy state in CB. In fact, in order for excitation or recombination to take place, the phonon momentum must be preserved so that $\Delta k = 0$.

To summarize the difference in band transitions of indirect and direct bandgap semiconductors: the former requires a change of phonon momentum, while the latter prohibits

it. Figure 2.6 gives an example for relaxation in direct and indirect bandgap semiconductors, which depicts photons as purely energetic transitions whereas phonons are given as a separate variable as wave momentum.

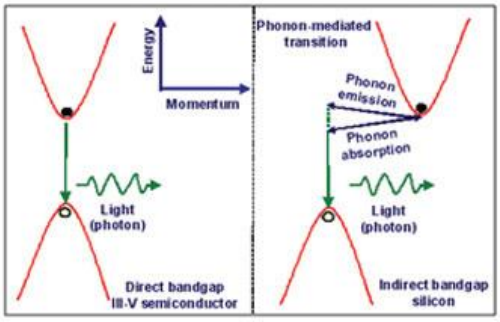

Figure 2.6: Lowest energy bandgap transitions for indirect and direct semiconductors. The former requires a phonon momentum component, while the other does not.

In other words, direct bandgap semiconductors do not benefit from phonon momentum at all. Any phonon contribution to state transitions will be lost as heat when the excited electrons reach their most stable state. Likewise, an indirect bandgap semiconductor such as silicon will always waste energy in the form of heat whenever an electron relaxes back to the VB.

2.1.4 Intrinsic and extrinsic semiconductors

In order to obtain adequate electric properties for a solar cell, charge carriers must be readily available for excitation and conductance through a circuit. In a semiconductor the charge carrier is a quasi-particle called an exciton, which consists of a negative electron and the positively charged void it leaves as it is displaced it the solid by an electric field. For the sake of simplicity, this electron void is called a “hole” in scientific literature.

When excited to the CB and delocalized, an electron will leave behind a hole that propagates in the opposite direction when influenced by an electric field. A pure semiconductor is “intrinsic” in the sense that it has no foreign elements that alters its conductive properties. In the case of silicon, one of its 4 valence electrons must break from its lattice bond to contribute to the overall current, leaving behind a hole in the process that propagates in the opposite direction to the electron. Cleaving chemical bonds in this manner is energy intensive and not very efficient. This explains why conductivity in semiconductors increases with temperature:

thermal excitation of electrons occurs when covalent Si-Si bonds are given sufficient energy to be cleaved, thereby releasing free electrons. Since electrons and holes are created pairwise in an intrinsic semiconductor, the total conductivity σ in the material is given by both particles:

$$\sigma = qn\mu_n + qp\mu_p \qquad (2.3)$$

Where q is the elementary charge ($q = 1{,}6 * 10^{-19}C$), n and p are the concentration of electrons and holes, respectively. Also, μ signifies the mobility of each charge carrier. However, the pairwise generation of electrons and holes means that

$$n = p = n_i \qquad (2.4)$$

at thermodynamic equilibrium in an intrinsic semiconductor. Therefore, the total conductivity in an intrinsic semiconductor is only given by charge mobility, which is affected by temperature. Augmenting lattice vibrations by supplying heat to the semiconductor will increase the frequency at which covalent Si-Si bonds are broken, but despite increased carrier concentrations the conductivity will decrease at high temperatures when the vibrations impedes carrier movement.

An extrinsic semiconductor is created by implementing foreign elements into the crystal structure, thus introducing new energy levels that improves conductivity. All semiconductors used for PV applications contain precisely controlled amounts of select impurities, called dopants. Without dopants, the rate at which a solar cell generates charge carriers would have been insufficient for power generation. Unlike its intrinsic counterpart, the conductivity in an extrinsic semiconductor does not increase much with temperature. This is because charge carriers from the implemented dopants are now the main contributor to the semiconductor's conductive properties. Moreover, crystal lattice vibrations will become a hindrance to charge carriers at high temperatures, thus reducing conductivity. If electrons have been added to the semiconductor by doping so that $n \gg p$, then equation 2.3 simplifies to

$$\sigma = qn\mu_n \qquad (2.5)$$

Similarly, if the concentration of holes increases by doping so that $n \ll p$, their contribution to the overall conductivity will dominate and equation 2.3 reduces to

$$\sigma = qp\mu_p \qquad (2.6)$$

The introduction of new energy levels causes a shift in the Fermi level, thus resulting in a higher frequency of excitation compared to that of the intrinsic semiconductor. The process of

introducing foreign elements to alter electric properties is called doping and will be described more in detail in the following section.

2.1.5 Dopants: n-type and p-type semiconductors

The dopants introduced into an extrinsic semiconductor must possess an atomic size similar to the solid matrix to avoid material strain. In the case of silicon, the most commonly used dopants are boron and phosphorous.

Boron has 3 valence electrons compared to 4 in silicon, thus contributing with a positive charge carrier in the form a hole when covalently bound to silicon. Phosphorous have 5 valence electrons and introduces an excess electron a negative charge carrier. Thus boron is called an acceptor (of electrons) and phosphor is a donor (of electrons). Charge carriers that these dopants confer to the semiconductor can readily travel through the semiconductor compared to electron and holes in an intrinsic semiconductor. This is because donor electrons do not contribute to forming any bonds and are thus easily displaced, whereas holes are vacant sites that nearby electrons will occupy in an attempt to attain stability. Phosphorus and boron are shown in figure 2.7 together with their dopant electron and hole.

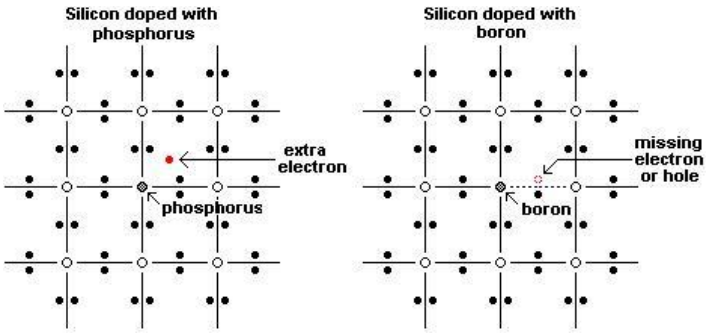

Figure 2.7: Doping by phosphorus and boron in silicon. Phosphorus confers an additional electron to the semiconductor while boron has one less than electron in its valence band. Both contribute to conductivity.

As mentioned in the previous section, electric properties of extrinsic semiconductors are principally dominated by their dopants as these contribute the most to the total current that these materials can create.

Thus silicon doped with boron is a p-type semiconductor where positive holes contribute the most, whereas silicon doped with phosphorous contributes with an electron and is therefore

called an n-type semiconductor. Consequently, holes and electrons are majority charge carriers in p-type and n-type semiconductors, respectively. Minority charge carriers also exist as excess holes in n-type and electrons in p-type. Although their concentration in the extrinsic semiconductor is far less than the majority carrier, they do contribute to the rate at which majority charge carriers are lost. To better understand how dopants improve conductivity in semiconductors in terms of energy states, it is useful to consider figure 2.8.

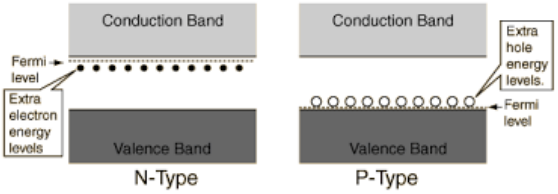

Figure 2.8: Implanted energy levels in n-type and p-type semiconductors.
Inserted n-type elements create a filled energy state near CB, while p-types create an empty energy state near VB.

As exemplified in figure 2.8, the creation of a p-type semiconductor by implementing boron into silicon creates a new energy state close to VB that is filled with holes. This shifts the Fermi level closer to VB, which augments the probability of electron excitation to this band. When electrons in a p-doped semiconductor excites to the empty dopant band by a photon, a hole is created in VB. A nearby electron will attempt to fill the vacancy in VB and in doing so will propagate the hole through the semiconductor. The empty dopant band effectively acts as a substitute CB. Phosphorous in an n-type semiconductor, on the other hand, creates a filled band near CB and naturally shifts the Fermi energy level closer to this band. The effective E_g between the phosphorous dopant band and CB is much smaller than that of an intrinsic semiconductor, thus requiring little energy for all dopant electrons to transition to CB and improve conductivity. In both cases a dopant atom only contributes with one charge carrier, hence a significant concentration of either acceptors or donors must be injected into the semiconductor in order to convey an appreciable change in conductive properties.

2.1.6 Solar cell structure

The fundamental technology of solar cells is relatively simple[6]. The surface on which photons impinge is coated with glass both to protect the layers underneath and improve light

refraction. Covering the electrically active are of the solar cell is an anti-reflecting coating (ARC) that maximizes photon absorption while at the same time preventing light that is reflected off the semiconductor from escaping. Electrically active areas of the cell are essentially junctions consisting of alternating layers of p-type and n-type semiconductors. Finally, metal contacts allow extraction of charge carriers from the solar cell. The simple pn-junction architecture of conventional silicon solar cells is illustrated in figure 2.9 below.

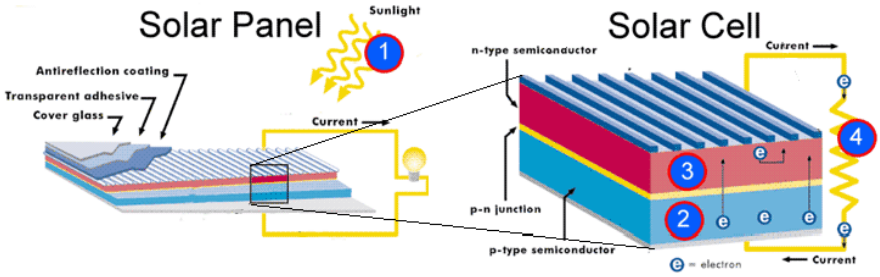

Figure 2.9: A conventional solar cell architecture. Impinging sunlight (1) excites charge carriers in the space charge region, which is electrons in the p-type (2) and holes in the n-type (3). They pass through the circuit (4) to generate power.

An electric potential appears at the junction interface which is caused by the charge concentration gradient appearing from majority charge carriers, (e.g. holes in a p-type semiconductor and electrons in n-type semiconductors). As soon as the junction is formed, charge carriers near the interface will diffuse across and into the semiconductor with an opposing polarity in an effort to cancel this electric potential difference and attain charge neutrality. Because this migration of charged particles is generated by difference in polarity between semiconductors, the attraction that a certain particle experiences will diminish with distance from the junction. For example, holes from boron atoms in the p-type semiconductor near the interface are more strongly affected by this potential difference than holes further away from the junction interface. Thus the holes near the junction interface will diffuse into the opposing, negatively charged n-type semiconductor, thereby leaving behind a negative charge at their origin. Electrons in the n-type semiconductor behave identically, leaving behind holes near the interface as they diffuse into the p-type semiconductor.

At thermodynamic equilibrium a space charge region has been established at the junction interface which serves to as a barrier to cancel any further charge diffusion. This barrier is shown in figure 2.10 with the polarities of each side.

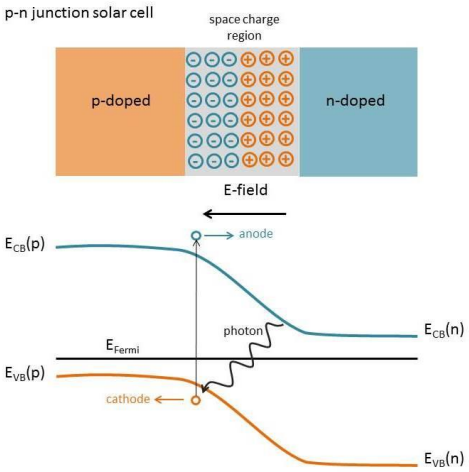

Figure 2.10: Electric potential diagram and schematic of the pn-junction.
Impinging photons excite electrons in the space charge region whereupon they become swept away by the electric field. Electrons are drawn towards the anode and holes are drawn towards the cathode.

The space charge region can be broken down in two ways. One way is by subjecting the pn-junction to a forward electric field, thus causing electrons in the p-type semiconductor to drift towards the positive anode. On the other side the holes in the n-type will drift towards the negative cathode. The other way is the one through which solar cells generate electric power from sunlight; by causing photons to excite electrons and holes in the space charge region. They will drift in opposite directions to preserve charge neutrality and finally be extracted through an outer circuit.

2.1.7 Carrier generation and recombination in silicon

In semiconductor science the process of creating an electron-hole pair by photon-induced excitation is called generation. The reverse process is called recombination and occurs when excited charge carriers spontaneously revert back to their original state by combining with a charge carrier of opposite charge. Recombination of holes and electrons causes the release of energy and may either be direct or through an intermediate energy state created by

impurities or defects. Whenever there is a generation process in a semiconductor, the spontaneous recombination process will be invariably present and proportional to generation.

The fact that charge carriers recombine and release energy means that recombination contributes to power loss and unavoidable heat generation in silicon solar cells. The rate at which generation and recombination occurs are both proportional to minority charge carrier concentrations. Those are electrons in p-type and holes in n-type semiconductors. The more excess charge carriers are present, the higher is the probability of recombination and generation to occur.

Several types of recombination occur in solar cells and the following subsections will explain the theory behind band-to-band, trap-assisted and Auger recombination. Their simplified mechanisms are illustrated in figure 2.11.

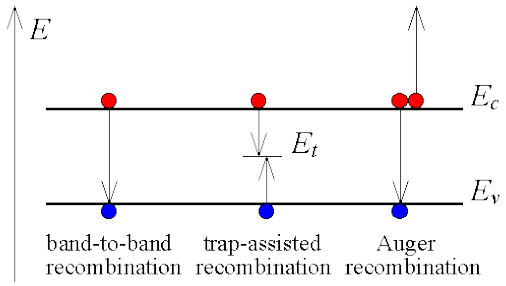

Figure 2.11: Recombination mechanisms of electrons (red) and holes (blue) in a semiconductor.

It should be noted that all the recombination mechanisms are present in a semiconductor. Moreover, the energy released as a result of all three recombination mechanisms can either be in the form of photons, or as vibrational energy given to the crystal lattice as phonons. In the latter case for phonon creation, these forms of recombination are jointly termed thermal recombination as opposed to thermal generation, which was mentioned in chapter 2.1.2. In short, recombination of charge carriers will inevitably contribute to heating and energy loss in solar cells. This is especially the case for indirect solar cells where recombination always produces phonons. When a solar cell is in thermodynamic equilibrium, e.g. not under illumination, the net carrier generation is zero because recombination and generation are performing together at equal rates.

2.1.8 Band-to-band recombination

Band-to-band recombination, also called radiative recombination, occurs when an excited electron falls from CB back to an empty state in VB and combines with a hole in the process, as shown in figure 2.11. This recombination mechanism requires both holes and electrons to be present and in the vicinity of one another. The result of a successful band-to-band recombination is in most cases only a photon whose energy is identical to the bandgap, E_g.

Consequently, this recombination mechanism conserves phonon momentum ($\Delta k = 0$). In other words, this recombination mechanism is one of the predominant manners through which energy is lost in a direct bandgap semiconductor.

Band-to-band recombination is only a minor cause of power loss for indirect bandgap semiconductors like silicon. Bandgap transitions in this type, both generation and recombination, require precise change in phonon momentum ($\Delta k \neq 0$) and thus the probability of either transition is considerably reduced.

Radiative recombination rate U in p-type and n-type semiconductors, respectively, can be simplified to the following expressions if the semiconductor is strongly doped:

$$U_{p,rad} = \frac{n_p - n_{p_o}}{\tau_n} \qquad (2.7)$$

$$U_{n,rad} = \frac{p_n - p_{n_o}}{\tau_p} \qquad (2.8)$$

In which τ is average lifetime of charge carrier prior to recombination. n_{p_o} and p_{n_o} are initial concentrations of minority carriers in p–type and n-type semiconductors, respectively, whereas n_p and p_n are charge carrier concentrations after recombination. Recall that a minority charge carrier is a charge carrier type that has a lower concentration in a doped semiconductor compared to a charge carrier of opposite charge. For example, a hole is a minority carrier in an n-type semiconductor where electrons dominate as charge carriers. The concentration of a minority charge carrier can be increased by adding more dopants of opposing charge to the semiconductor. Furthermore, note that equations 2.7 and 2.8 are only viable if the semiconductor is strongly doped with either dopant type. Even though this model is simplified,

it signifies that band-to-band recombination rate in a direct semiconductor is proportional to minority carrier concentrations.

2.1.8 Trap-assisted recombination

This recombination mechanism also called Shockley-Hall-Read (SHR) recombination. It is a non-radiative recombination mechanism that becomes prevalent when impurities create new energy states close to the semiconductor's Fermi level. Such energy states function as "traps" for charge carriers, hence the name. Recall from section 2.2 and equation 2.1 that the probability for an electron to be found at a certain energy level E increases as $E \rightarrow E_{VB}$. Thus electrons have a high probability of being excited to trap states near VB and up to E_F by small energy quanta, typically phonons or low-energy photons. Consequently, this reduced the excitation rate to CB. Trap-assisted recombination also occurs when an excited electron in CB and hole from VB meet at the trap energy state, releasing energy as result. Although an energy level intermediate to E_g can potentially increase carrier generation by stepwise excitation with photons of lower energy, this benefit is offset by increased recombination frequency.

An electron that has been excited into an intermediate energy level near E_F has a considerable probability of reverting back to VB, thereby losing energy in the form of a phonon. Electrons that have already reached CB can also undergo stepwise recombination by passing through the trap energy level. For this reason, trap-assisted recombination is one of the most detrimental means through which indirect bandgap semiconductors and silicon solar cells reduce photon conversion efficiency. Due to the inevitable presence of impurities in mc-Si, this recombination mechanism is the one that severely inhibits power generation in multi-crystalline solar cells. The trap-assisted recombination rate U_{SHR} is therefore defined as:

$$U_{SHR} = \frac{pn - n_i^2}{\tau_{n,SHR}(p + p_t) + \tau_{p,SHR}(n + n_t)} \qquad (2.9)$$

Where $\tau_{n,SHR}$ is the lifetime for electron capture by a trap energy level and $\tau_{p,SHR}$ is the case analogous to holes. p_t and n_t are concentrations of holes and electrons when their Fermi levels are equal to the trap energy level, respectively $E_t = E_{F_p}$ and $E_t = E_{F_n}$. Assuming that the semiconductor is strongly doped so that $n \gg p$ or $n \ll p$, the SHR recombination rate can be simplified to equation 2.7 or 2.8, respectively.

With some modifications the SHR model can also account for recombination by defects such as grain boundaries and line defects. Sites like these contain impurity precipitates and free

semiconductor atoms that are readily available to minority charge carriers traversing between crystal grains. In this sense a high concentration of grain boundaries or defects can promote recombination and have an adverse effect on performance. Crystal defects that contribute to recombination will be detailed in a later subsection.

2.1.9 Auger recombination

Auger recombination occurs when two holes or two electrons collide, whereupon one carrier is given the kinetic energy of the collision while the other falls down to a lower energy level to recombine with a carrier of the opposing charge. For example, two electrons can collide in CB, one of them absorbs the kinetic energy of the other and the less energetic electron falls back to VB where it recombines with a hole. The excited electron has no higher energy state it can reach and will shortly thereafter fall back to its initial energy level in CB, while relinquishing its extra energy as heat through thermalizing. The complete expression for Auger recombination is

$$U_{Aug} = U_{Aug,n} + U_{Aug,p} \qquad (2.10)$$

$$U_{Aug} = \Gamma_n n(np - n_i^2) + \Gamma_p p(np - n_i^2) \qquad (2.11)$$

Where Γ_n and Γ_p are Auger coefficients for electrons and holes that are specific to the semiconductor. As the expression implies, Auger recombination is most prevalent in strongly doped materials or at high temperatures, which in both cases means high carrier concentrations and hence high frequency of collisions. Interestingly, Auger events conserve both energy and momentum regardless of whether the material is an indirect or direct semiconductor. This preservation of both energy and momentum in an indirect semiconductor can be explained by accounting for symmetry. If both colliding electrons in CB have an initial momentum k and the change in momentum is Δk, the electron that becomes demoted to VB will have its momentum reduced by $(k + \Delta k)$ while the promoted electron's momentum is increased by $k + \Delta k$. The net change in momentum after this recombination is therefore zero. This property ensures that Auger recombination occurs for both indirect and direct semiconductors, thereby causing a decrease of carrier lifetimes as their concentrations increase. Hence this recombination mechanism serves as a final limit for carrier densities and solar cell power output.

2.1.10 Light induced degradation

Light induced degradation (LID) of solar cells occurs when dopant elements and impurities form complexes with one another, which is facilitated by a bias voltage or illumination. Dopants that form complexes use their electrons to form strong covalent bonds, which, as a result, do not contribute to the cells photon conversion and therefore constitute an efficiency loss. LID is especially observed in p-type mc-Si and c-Si solar cells with high oxygen contamination, in which formation of interstitial B_iO_{2i} complexes form under illumination[7]. As will be detailed in a later subsection, contaminants like oxygen and carbon are introduced in mc-Si ingot production. This phenomenon is also called carrier induced degradation (CID) since the same behavior is observed whenever strong charge generation occurs.

For c-Si solar cells these complexes may degrade photon conversion by up to 10%, whereas only 2-3% in oxygen rich wafers of mc-Si. Other impurities such as interstitial iron can form a FeB complex with substitutional boron, although their bond dissociate under strong illumination. These complexes reappear if the solar cell remains inactive for extended periods of time, thus reducing overall efficiency considerably. However, as industrial processes become increasingly proficient at reducing impurities in mc-Si and improving crystallinity, LID impose considerable performance limitations in p-type wafers. Post-production treatments that remove crystal defects, like thermal annealing above 200 ℃, seems to break down these complexes[8], However, this is only a temporary solution due to internal diffusion of impurities.

2.1.11 Impurities and compensation

Introduction of new elements to a semiconductor will create new energy states. Some elements are added in precise amounts and confer beneficial electric properties to the semiconductor as dopants. The most common dopants used in solar cell industry are boron and phosphorus. However, other elements like oxygen, carbon, nitrogen and transition metals are incorporated by diffusion at elevated temperatures during semiconductor production. Such diffused impurities are almost impossible to avoid when solidifying mc-Si and will reduce the solar cells effectivity because they reduce the rate at which charge carriers are successfully excited to CB. This effect of trap-assisted recombination was covered in section 2.7.2. The concentration of such harmful impurities are difficult to avoid, and given that every element in a doped semiconductor adds unique energy states, the purity and control of material composition quickly becomes a limiting factor to solar cell effectiveness. As shown in figure 2.12, more impurities present in a solar cells means more available energy states of different magnitude.

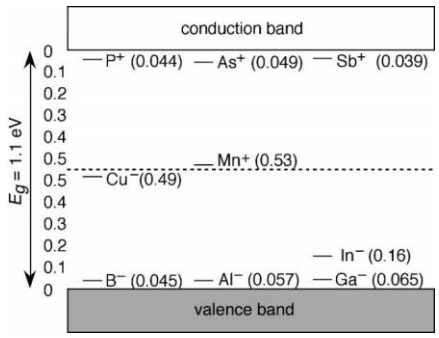

Figure 2.12: Energy bandgap of silicon with impurities. Impurities create additional energy levels that compete with those created by dopants like boron and phosphorus.

Many elements from group III and group V in the periodic table have energy levels similar to those of boron and phosphorus, respectively. Impurities from group III have 3 valence electrons and thus contribute with holes to the semiconductor. Group V elements contribute with electrons. Other impurities, such as transition metals copper and manganese, introduce new energy levels that are closer to silicon's Fermi energy and act recombination sites. Considering that new energy levels may allow the semiconductor to absorb more photon wavelengths, it would appear that creating multiple energy levels could improve solar cell photon conversion and thus ameliorate cell performance.

However, this is not the case. If donor and acceptor dopant atoms are in vicinity of one another, the probability of donor electrons being used to reconstruct broken bonds in acceptor atoms increases. Such electrons are not easily removed and are essentially lost as charge carriers. In fact, the formation of dopant complexes in this manner is one of the most prevalent issues when producing solar grade silicon. As has been mentioned earlier, the dopant atoms in a solar cell are the principal contributors to charge carriers. Therefore, the loss of electrons and holes by formation of complexes means that power generation will diminish greatly. This is especially the case if complexes form in the solar cell's space charge region, which is the principally active area.

Since impurities either add more holes or electrons to the semiconductor, their incorporation alters the net amount of available charge carriers. For example, adding more phosphorus to a p-type semiconductor will effectively reduce the total amount of available charge carriers because more electrons will recombine with holes. Recall equation 2.6 for this particular case. This reduction of conductivity by equalization of charge carrier concentrations

is called compensation and may greatly affect a solar cells ability to generate power. Fortunately, compensation may be remedied by increasing the concentration of either holes or electrons by doping, thus making the semiconductor predominantly n-type or p-type again.

2.1.12 Material defects in silicon

Dislocations and defects are always present in mc-Si and in greater magnitude than c-Si. Their creation can be explained by plastic deformation of the silicon ingot at elevated temperatures ($T > 800\ ^{o}C$) due to thermal expansion and subsequent strain from the crucible walls.

As their formation is promoted by plastic deformation of the ingot and grain collision, they exist in abundance near crucible sidewalls and increase in density as the ingot grows. Coupled with the fact that impurities diffuse from the crucible walls, this causes dislocations to act as favorable sites for impurity accumulation and precipitation. Consequently, dislocations greatly limit the carrier lifetime in mc-Si, especially near the crucible walls and ingot top where growing grains converge. These regions are aptly named “red zones”. A standard procedure in decreasing red zones and annihilating defects is ingot annealing. This subchapter describes the types of material defects that appear in mc-Si and how they are connected to mechanical and conductive properties.

Point defects

Point defects are caused by removal or displacement of single atoms. Inclusion of impurities can either substitute an atom in the crystal lattice or be placed interstitially in the crystal. The former is most common for impurities with an atomic size similar to that of the host atom, whereas the latter occurs for smaller impurities. Therefore, most oxygen impurities occupy interstitial sites whereas carbon substitutes silicon. Lattice vacancies and self-interstitials are some of the most common point defects and can be found in any crystal. Vacancies are empty lattice sites in a crystal, while self-interstitials appear when an atom of the host element has diffused and placed itself into a void space normally left unoccupied.

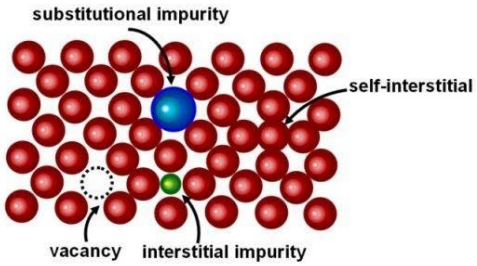

Figure 2.13: Point defects in a crystal lattice. Vacancies and self-interstitials appear readily in the crystal due to stacking faults, whereas substitutional and interstitial impurities require that the atomic radius is similar to that of the host atom.

Linear defects

Linear defects are two-dimensional misalignments of lattice spacing and can be classified into two types that often appear in tandem as a mixed dislocation. Edge dislocations appear as extra half planes within a crystal that shift neighboring planes internally. The end of the half planes has dangling bonds along their edge which act as recombination sites and add local strain to the crystal lattice. Edge dislocations can be cancelled by propagating the half-plane out of the crystal or through removal of the dangling bonds by combining two opposing half planes. The other type of linear defect is a screw dislocation in which crystal planes are shifted normal to the crystal surface, thus creating a protruding atomic ledge.

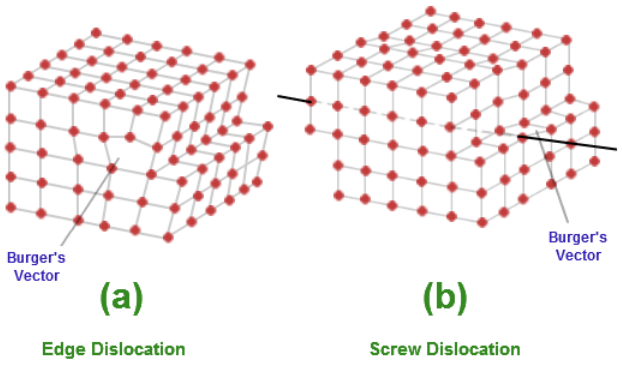

Figure 2.14: Linear defects in the form of (a) edge and (b) screw dislocations.
The edge dislocation appears as an inserted half-plane, whereas the screw dislocation is given as a slip or misplacement between two planes. Burgers vectors are traced around both linear defects in order to visualize the degree of dislocation. In both cases the Burgers vector indicates one plane of defect.

Interfacial defects

A region where crystallographic orientation is different among several parts of the crystal is called an interfacial defect. These defects appear as grain boundaries, surfaces, phase boundaries or twinning boundaries. A multi-crystalline solid is riddled with these species of defects compared that a crystalline solid, which explains why their mechanical and electric properties can be very different.

Grain boundaries occur naturally in multi-crystalline solids. The term “grain” implies that a certain area of a solid exists separate to that of adjacent parts of the solid. In this sense a grain has a degree of misalignment to adjacent grains which is caused by a different crystallographic orientation. Grains with a low degree of misalignment are called low angle boundaries, whereas grains with a high degree of mismatch are naturally called high angle boundaries. One of the principal reasons as to why grain boundaries are detrimental to electric conductivity lies in the irregularity of atoms at these interfaces. Dangling bonds are frequent and act as trapping sites for charge carriers and tend to accumulate impurities in the form of precipitates. The latter case has been studied by Autruffe *et al.*[9], whose results with copper decoration at grain boundaries demonstrate that transition metal impurities concentrate at highly mismatching boundaries. Consequently, high angle boundaries are more active than low angle boundaries due to a higher number of dangling bonds.

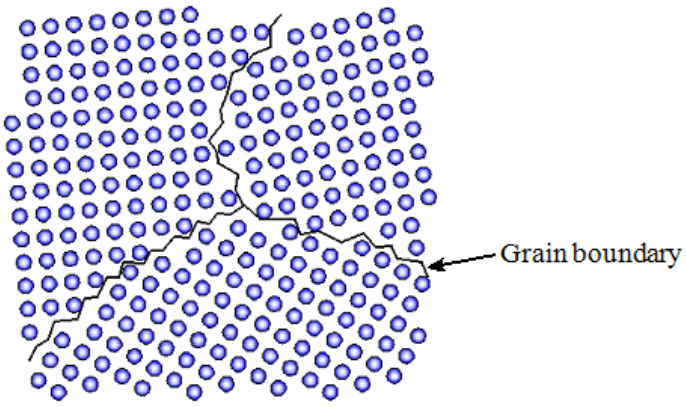

Figure 2.15: Grain boundaries in a non-crystalline solid.
The grains are indicated by a blue outline and have mutually mismatched crystallographic orientations. The degree or mismatch is given as the angle between identical crystal planes. As can be seen in the figure, the center grain has high angle boundaries with adjacent grains.

A variant of grain boundaries is the twin boundary, in which two grains are not separated by dangling bonds. Instead, the end face of one grain also acts as the beginning of the adjacent grain's face. Due to a lack of dangling bonds a twin boundary does not contribute notably to efficiency loss in mc-Si solar cells.

One of the major drawbacks of mc-Si over c-Si is its high density of point, linear and interfacial defects. While c-Si has an average defect density of 500/cm^3, mc-Si can have as much as 10^6/cm^3. A crystallographic defect is a lattice irregularity in the order up to a few atom diameters[10]. Areas in which defects are occurring effectively function as trapping sites, thus increasing wafer resistance. This section presents an overview of the most common crystal defects to be found in mc-Si.

2.1.13 Summary

Semiconductors are well suited to photovoltaic power generation due to their relatively small bandgaps, which can absorb single wavelengths of light as energy quanta. Their conductivity will increase substantially through either p-type or n-type doping, in which foreign elements confer additional holes or electrons to the semiconductor, respectively. Such semiconductors are denominated as extrinsic semiconductors, as opposed to pure semiconductors that are so-called intrinsic. Compared to intrinsic semiconductor, an increase in temperature does not largely increase conductivity in extrinsic semiconductors. However, the incorporation of foreign elements must be carefully controlled as they contribute to increased recombination rate in silicon, which is the main cause of power loss in solar cells. Impurities tend to accumulate at defect sites like grain boundaries, or may be incorporated into the crystal lattice as substitutional or interstitial atoms. As impurities enter the silicon ingot through diffusion during silicon ingot production, it is imperative to control processing parameters such as temperature and growth rate. The incorporation of impurities and details of silicon ingot production will be the focus in following sections.

2.2. Growth of multi-crystalline silicon

Production processes for multi-crystalline and crystalline silicon for solar cell applications share many of the same parameter criteria to achieve acceptable performance, yet their setup can be very different. While solar grade mc-Si production is largely dominated by the simple directional solidification process, most c-Si is produced by the relatively complex Czochralski process. As mc-Si is the interest of this project, the principles of its conception is the focus of this section. Firstly, the directional solidification process itself will be covered to give a clear understanding of how mc-Si ingots for solar cell applications are manufactured. Following this will be theory and findings that explains how separate process parameters influence material quality in terms of crystallinity, purity and performance. Unless specified otherwise the theory in this chapter has been extracted from Handbook of Crystal Growth: Bulk Crystal Growth[11].

2.2.1 The directional solidification process

Directional solidification[12], otherwise known as the Bridgman-Stockbarger technique or the vertical Bridgman technique, is among one of the most common production processes of metal and semiconductor ingots due to its scalability and economic handling. The influence of process parameters like temperature and pulling rate is well known, and the throughput of mc-Si ingots is also quite high compared to the Czochralski process. However, these benefits come at the price of material quality and purity. To understand the process as a whole, it would be useful to study figure 2.13 and go through it stepwise with respect to equipment and handling commonly used in the industry. A basic directional solidification process can be divided into four segments:

- Heating the susceptor to above melting temperature $T_m = 1410\ ^oC$.
- Melting at constant temperature.
- Ingot solidification at constant cooling rate through vertical heat flow.
- Cooling to room temperature.

Firstly, prior to the solidification process itself, a heated melting crucible made of fused quartz is evenly spray-coated with a slurry of silicon nitride and then left to dry. The coating prevents sticking of silicon to the crucible, while fused quartz is used as crucible material because of its compatibility with silicon. How the choice of crucible material and coating affects the ingot will be elaborated in the following subsections. After coating and drying the crucible

is loaded with solar grade silicon together with a certain quantity of dopants, be it boron or phosphorous, and put in a graphite case which acts as an insulator. Depending on what type of mc-Si ingot one intends to manufacture, the silicon has either been placed directly into the crucible or over a seeding layer that facilitates crystal growths. In the latter case the heat influx must be controlled accordingly to prevent melting of this seeding layer while successfully melting the silicon charge. The silicon is now installed in the furnace and preparatory measures can be performed. First of all, the crucible with its surrounding case is covered by a graphite plate with a tube connected to the top. The furnace is vacuumed through the tube, then purged with argon gas to prevent any contaminant gases to be present prior to melting. During the melting phase, a susceptor above the insulating graphite cask is heated by induction coils and transfers radiative heating to the crucible under an argon gas phase. Argon gas is continuously pumped into the furnace to evacuate any gases evaporating out of the melt. Internal heat of the system is can be controlled by several mechanisms, depending on the furnace model. One way is by varying the amount of heating from the susceptors above the melt while at the same time lowering the crucible base temperature through convective heat transfer. Water flowing through a hollow copper plate is often used. Another is to utilize a gas heat leak system, usually consisting of insulating carbon fiber disks through which argon gas is pumped and exchanges its heat with a cooling element. Relative rotation of these disks ensures that ventilation can be partially or completely opened to adjust heat evacuation. Vents like these are usually placed at the bottom of the system, just above the water cooled copper plate. A third option is to vertically lower the crucible gradually in order to create a temperature gradient between the melt phase and solid phase, which crystallized from the bottom up. Lastly, these mechanisms can also be used in conjunction with one another to gain better control of the crystallization rate. However, the Crystalox DC250 furnace used in to solidify ingots for this thesis employs an active cooling system that consists of circulated argon gas that removes heat convectively with a water-cooled heat exchanger, as proposed by Li *et al*[13]. A system like this was deemed most useful to preserve a seeding layer of silicon, which was also used in the project.

Melting and cooling of silicon is accurately controlled by using a pair of thermocouples. One is places directly above the susceptor and is a means of detecting power output and heating, the other is placed beneath the center of the cooling element. During the melting stage the temperature at the upper thermocouple increases quickly to above T_m. As heat is transmitted through the silicon charge, the temperature at the lower thermocouple will begin to rise. It should be noted that larger pieces of silicon will melt more slowly than smaller pieces and may therefore be suspended in the melt. In addition to this, a melt will experience some temperature

fluctuations due to gas evaporation, natural convection and because floating pieces of silicon absorb heat while shrinking. Solid silicon, on the other hand, does not exhibit temperature fluctuations as it absorbs heat steadily. Therefore, a consistent temperature fluctuation at the lower thermocouple is an indication of complete melting. At this point the heating is reduced and growth is initiated by distancing the heating element or by reducing its heat output. As heat is evacuated through the bottom section, the ingot crystalizes upwards at a steady rate of 1-2 cm/h. Figure 2.16 illustrates this stage of the process.

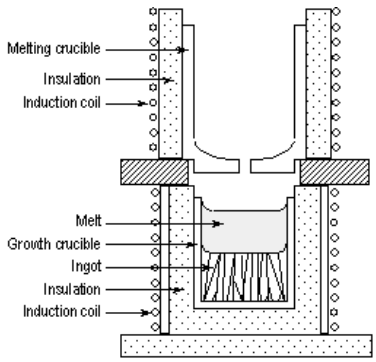

Figure 2.16: Directional solidification of an ingot. This particular setup uses a stationary, insulated crucible where the vertical temperature gradient is created by modulating heat from induction coils

At this point of the process it is crucial to control the temperature gradient and growth rate, otherwise defects and dislocations are prone to develop. Also, as the ingot cools down the silicon becomes increasingly brittle. Cooling too fast implies a risk of breakage due to elastic thermal stress from the crucible. When the ingot has been completely solidified the insulating graphite plate is lowered and the annealing stage begins. During annealing the temperature at the bottom is increased so that the temperature is uniform and below 800 ^{o}C throughout the ingot. Annealing is an important processing step that allows the ingot to alleviate dislocations and thermal stress. However, because annealing is performed at elevated temperatures, impurities from the crucible and graphite insulation will diffuse into the ingot. The whole ingot growth cycle takes approximately 60 to 70 hours, of which melting constitutes about 20 hours. Time of crystal growth depends on the desired growth rate and how the ingot is annealed and cooled down. After crystallization the ingot is sawed and sectioned prior to wafering.

2.2.2 Crucible material and coating

As was mentioned in the previous section, the use of silica as a crucible material is the industry standard for mc-Si production through the directional solidification technique. Silica as a crucible material possesses many features that are attractive for ingot growth. First of all is has good mechanical strength and is able to withstand high temperatures due to its thermal shock resistance. Secondly, it is a highly pure material that consists mostly of silicon and oxygen. Thirdly, it has an exhibits little thermal creep at high temperatures and is a good insulator. However, despite being the most frequently used crucible type, its use is limited to a single time. This can be explained by a solid phase transition and the subsequent stress it causes on the ingot. Initially, silica has a glassy microstructure that persists up to high temperatures. When the crucible temperature exceeds 1200 ^{o}C, however, the outer shell of glassy silica grains begins to melt and rearrange themselves in a process called sintering. As the crucible temperature is sustained over long time, the crucible undergoes some creeping due to devitrification where the glassy phase melts away. When the temperature rises above 1450 ^{o}C during the melting stage, devitrification and creep increases and silica begins to transform into the more rigid β-cristobalite phase. The crucible retains a considerable amount of inclusions of this phase until the cooling stage, where it transforms to α-cristobalite near 275 ^{o}C. α - cristobalite is less dense than β-cristobalite and will therefore expand, thus causing mechanical strain that may result in breakage of the crucible.

Another issue with silica crucibles is wetting by solidifying silicon. A liquid is said to be wetting on a specific substrate if its drops form a low contact angle $\theta_C < 90^o$ on the surface. On the other hand, if the drops have a contact angle $\theta_C > 90^o$, they are said to be poorly wetting. In the intermediate case when $\theta_C \approx 90^o$ the liquid is said to be partially wetting. This behavior can be explained by the relationship that arises between interfacial energies of different phases. Interface energies between the solid-gas phases, γ_{SG}, the solid-liquid phases, γ_{SL}, and the liquid-gas phases, γ_{LG}, are balanced at thermodynamic equilibrium. Figure 2.17 gives an example of a partially wetting liquid on a substrate. According to Young's equation, the contact angle decreases with increasing substrate surface energy:

$$\cos\theta_C = \frac{\gamma_{SG} - \gamma_{SL}}{\gamma_{LG}} \qquad (2.12)$$

Liquid silicon has a contact angle of approximately 90^o on silica and is therefore partially wetting on the substrate[14]. In its molten form it expands into the upper layer of pores on the silica surface. As the melt cools down the silicon begins to contract due to its thermal

expansion coefficient, which is lower than that of silica. Consequently, an uncoated silica crucible will cause micro-fracture and act as a growth site for dislocations in the ingot.

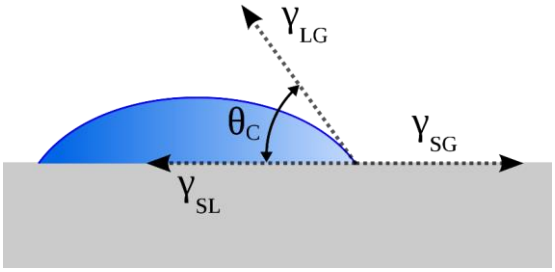

Figure 2.17: Interfacial energies between liquid-solid, liquid-gas and solid-gas determine the degree of wetting on a substrate.

Additionally, direct contact between liquid silicon and the silica crucible would facilitate oxygen diffusion. Despite being chemically stable at high temperatures, some silica will dissolve into the melt and cause oxygen contamination. Therefore, a high-purity crucible coating of silicon nitride is commonly used to prevent wetting of silicon, fractures and diffusion of impurities. In fact, the purity of both crucible and coating have a great impact on solar cell performance[(15)] in terms of minority carrier lifetime. Typically, the impurity content of Al, Fe, Ca and Ti is higher by several orders of magnitude in a silica crucible, relative to the silicon nitride coating. However, impurities in the coating *are* present and will diffuse into the during the melting stage. Transition metals like Fe, Cu, Ni and Co have high solubility and diffusion coefficients in liquid silicon and tend to accumulate along grain boundaries due to the increased surface energy at such sites. Defects and high density grain boundaries are prominent near the crucible walls, and as such these parts of the ingot will exhibit much lower minority carrier lifetime than the center due to recombination. Consequently, coating impurity content and diffusion control is imperative to obtain a defined center ingot.

While silicon nitride is the most used coating material, its contact angle with liquid silicon is greatly affected by impurities, especially oxygen. Even though silicon nitride is thermodynamically stable at elevated temperatures, it can be readily oxidized even at low oxygen partial pressures[(16)]. A high oxygen content in the form of silicon oxynitride relates to a high contact angle, thus a low degree of wetting. Unfortunately, this oxygen content tends to dissociate into the melt at high temperatures and low oxygen partial pressure in the form of SiO, subsequently increasing the degree of wetting with holding time. As verified by Drevet *et*

al.[17], this increased wetting and infiltration depth apply to pores where the coating pores have become deoxidized. Because the wetting increases with oxygen dissociation in porous coating, the melt will gradually begin to invade past the coating and stick to the crucible. This, coupled with the ensuing high-temperature phase transformation, ensures that each silica crucible can only be used once, even if the infiltration of silicon is only partial.

The limitation to single use of a silica crucible has created considerable interest in production of reusable crucibles. A reusable, less wetting crucible would reduce ingot production cost significantly, but as of now there is little documentation on use of such crucibles. Silicon nitride crucibles have been of considerable interest as they do not undergo solid phase transformations or creep like silica, making them very stable at high temperatures. However, some of the main challenges in commercializing a silicon nitride crucible lies in its physical properties and how they differ from those belonging to conventional silica crucibles. In terms of mechanical properties, the crucible must have a similar thermal expansion coefficient and thermal conductivity to that of silica. Bellman et al.[18] grew ingots in silica and silicon nitride crucibles, both coated with Si_3N_4. Their work showed that ingots grown in coated silicon nitride crucibles would require more heat during melting, but less during ingot growth. This was due to the thermal conductivity coefficient κ W/mK or silicon nitride being several times higher in than silica, especially at ambient temperatures.

Previously, one of the greatest drawbacks concerning silicon nitride ingots was the necessity for using binding agents to facilitate crucible sintering, as well as in silicon nitride coating[19]. Fortunately, advances in silicon nitride casting has eliminated the need for such impurity sources by creating NBSN crucibles that are made by isostatic pressing[20]. Such crucibles can be made with a porous structure, thereby reducing thermal expansion. Additionally, as demonstrated by Roligheten *et al*.[21], the composition can be altered to include silicon oxide to decrease wetting and give the crucible a thermal conductivity and thermal expansion comparable to a silica crucible while preserving its mechanical properties. These trends in crucible properties by composition were also investigated by Zhao *et al*.[22], whose results showed a flexural strength and thermal expansion displayed a linear relationship with composition. The potential of silicon nitride crucibles has been further demonstrated by Schneider et al[23]. who managed to growth 7 ingots in a single NBSN crucible without cracking. However, the same group discovered that ingots grown in NBSN crucibles displayed a higher level of B, P and Al contamination relative to standard silica crucibles. Their concentration remained high in the ingots even after multiple growth sequences. The same group also

documented that oxidation of internal and external pore structure was imperative to avoid melt invasion in NBSN crucibles[24].

2.2.3 Impurity segregation

As has been mentioned in previous chapters, the presence of impurities and dislocations decrease minority carrier lifetimes through recombination and are thus directly responsible for power loss in solar cells. Most impurities and defects in multi-crystalline solar cells are introduced during directional solidification. Carbon and oxygen are incorporated into the ingot through a series of reactions involving evaporation and dissolution, and will therefore be covered more in detail in the next subchapter. Transition metals like iron, copper, aluminium and chromium exist in the crucible and coating as trace elements or in binding agents, but can also be found in the silicon feedstock if it is low quality. Their inclusion, together with nitrogen from the coating, is purely through diffusion and can be detailed in two steps.

Firstly, impurities begin to diffuse into the melt because their solubility in silicon increases with temperature and liquefaction. Secondly, when the ingot grows due to a controlled temperature gradient, the impurities concentrate into the melt as their solubility and diffusivity is much higher in a liquid phase. Consequently, the impurities become "pushed" upwards as the ingot grows. However, should the melt become supersaturated with impurities at elevated temperatures, some will undergo back-diffusion into the ingot. This largely depends on the element's liquid diffusivity D_l, solubility S and equilibrium segregation coefficient k_0. Table 2.1 gives these parameter values for some of the most common impurities and dopants in directional solidification of silicon.

Table 2.1: The most common impurities in silicon and their equilibrium segregation coefficient k_0, solid solubility S and liquid diffusivity D_l

Element	k_0	S $[atoms/cm^3]$	D_l $[cm^2/s]$
O	1.25	$5.7 * 10^{18}$	$3.6 * 10^{-4}$
P	0.35[25]		
B	0.78[26]		$4 * 10^{-4}$[26]
C	0.07	$5 * 10^{18}$	$3.5 * 10^{-4}$
N	$7 * 10^{-4}$	$2.2 * 10^{18}$	$4.1 * 10^{-4}$
Cu		$1.1 * 10^{17}$	$8 * 10^{-5}$
Ni	$8 * 10^{-4}$	$3.5 * 10^{16}$	$1.6 * 10^{-5}$
Fe	$1.5 * 10^{-5}$	$1.2 * 10^{13}$	$1.2 * 10^{-6}$
Cr	$3.1 * 10^{-6}$	$1.7 * 10^{13}$	$3.6 * 10^{-7}$
Ti	$3.5 * 10^{-5}$	$1 - 7 * 10^{10}$	$7.6 * 10^{-11}$

Solubility is a measure of how many impurity atoms can be dissolved in the melt before precipitating, whereas the liquid diffusivity details the specie's ability to permeate into the melt from a solid or gas phase. The equilibrium segregation coefficient is of particular interest in the vertical solidification process. It denotes an impurity's ability to segregate into either a liquid or solid phase in a hot zone process, such as the Bridgman-Stockbarger process, at constant temperature and pressure. It is defined as:

$$k_0 = {}^{C_S}/_{C_0} \qquad (2.13)$$

Here C_S is the impurity concentration in the solid ingot and C_0 is its initial concentration in the melt. Thus impurity species with a low value of k_0, such as most transition metals, will segregate into the melt as the ingot grows. As can be verified from Table 2.1, this correlates with the specie's solubility and diffusivity. On the other hand, smaller elements like boron display a higher segregation coefficient. Assuming that there is no diffusion of species and that an equilibrium exists at the interface, the distribution of impurities in the liquid phase can be modelled by the Scheil equation:

$$C_S = k_0 C_o (1 - f_S)^{k_0 - 1} \qquad (2.14)$$

Here f_S is the height fraction of solidified silicon. Impurities that follow the Scheil equation will have concentrations that increase with ingot height. This is clearly demonstrated in Figure 2.18, which gives a transient representation of the Scheil equation in the middle of solidification.

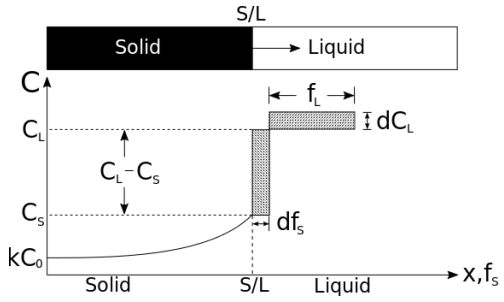

Figure 2.18: The Scheil equation.C_S and C_L are impurity concentrations in the solid and melt. f_S and f_L are their mass fractions.

The equation is a useful tool for predicting impurity concentrations, particularly for transition metals with low k_0 values, low solubility and low diffusivity. However, the equation does not account for the effect of ingot growth rate, melt convection and diffusion to the ingot-melt interface. This can be remedied to a certain extent by expressing an effective segregation coefficient k_{eff}[27]:

$$k_{eff} = \frac{k_0}{k_0 + (1 - k_0)exp(-\nu\delta/D_l)} \qquad (2.15)$$

Here ν is the ingot growth rate, δ is the boundary layer thickness and D_l is the aforementioned impurity diffusivity in molten silicon. The boundary layer thickness is defined as the region of the ingot-liquid interface where no convection or mixing currents occur. Because there is no stirring of the silicon melt, this parameter is a variable of natural convection caused by the ingot-melt heat gradient. Despite these corrections to the Scheil equation, it fails to accurately predict impurity concentration of species that exhibit $k_{eff} > 1$ or undergo back-diffusion from the top due to high diffusivity. This makes the model somewhat inadequate for modelling oxygen and iron concentration profiles, respectively. Additionally, it does not account for inclusions or precipitates in the ingot.

Some impurities have low solubility in silicon and will therefore tend to precipitate in the solid phase. This behaviour is observed in nitrogen, which forms needles or fibres of silicon nitride along grain boundaries when its solubility limit of 128 ppma is exceeded. These precipitates act as shunting sites and are thus detrimental for the electrical properties of the ingot, but their growth can be inhibited by improving melt convection and decreasing growth rate. Also carbon can form shunting precipitates in the form of carbon silicates. Carbon solubility in silicon is 100 ppma and will therefore often nucleate near or at silicon nitride precipitates. Oxygen, on the other hand, has a larger solubility than silicon and a similar atomic radius. It therefore occupies interstitial crystal lattice sites or, if sufficiently supersaturated in the melt, decorates grain boundaries to create precipitates of silicon oxide. Fortunately, oxygen impurities rarely exist in sufficient amounts to form precipitates.

2.2.4 Gas flows above melt

Impurities are incorporated into the silicon ingot during solidification through various mechanism, some of which can consist of many steps and be rather complex[28]. In the case of oxygen and carbon, this entails a series of reactions that are illustrated in Figure 2.19.

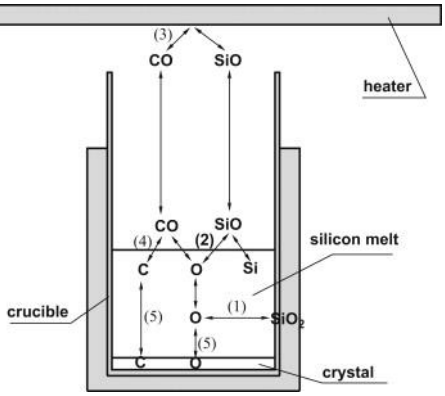

Figure 2.19: Crucible dissolution and incorporation of oxygen and carbon impurities in a directional solidification process. The figure is as reported by Gao *et al*.

Initially, oxygen impurities originate as the melt diffuses past the coating layer and begins to dissolve the silica crucible. Silica particles are then transported in the melt due to natural convection caused by temperature gradient between the growing ingot and melt, before evaporating from the melt surface as SiO:

$$SiO_{2(s)} + Si_{(l)} = 2SiO_{(g)} \qquad (2.16)$$

Unevaporated silica will remain in the crucible as precipitates or inclusions when the melt cools down. If the furnace has an argon gas flushing system installed, most of the evaporated gas will be removed. If the flushing is inadequate or not present, evaporated SiO proceeds to react with any graphite component, typically the heating element or insulating cask:

$$SiO_{(g)} + 2C_{(s)} = CO_{(g)} + SiC_{(s)} \qquad (2.17)$$

This is also the manner through which SiC precipitates are introduced to the melt. Pure carbon is introduced into the melt as carbon monoxide dissociates at the melt surface, thus reintroducing oxygen in the process:

$$CO_{(g)} = C_{(m)} + O_{(m)} \qquad (2.18)$$

Alternatively, the silica crucible can also react with the graphite insulation directly, thereby shortcutting the aforementioned evaporation-dissolution cycle:

$$SiO_{2(s)} + C_{(s)} = SiO_{(g)} + CO_{(g)} \qquad (2.19)$$

Because oxygen dissolves from the crucible surface, its rate of diffusion into the melt is proportional to the amount of silicon melt present. Therefore, its concentration in a standard directional solidification process is 5-10 ppma and decreases with ingot height. However, it can also back-diffuse into the crucible melt as a gas due to its high liquid diffusivity, thus causing it to deviate from the Scheil equation. Carbon, on the other hand, is introduced at the melt-gas interface and therefore its standard concentration is near 7 ppma and decreases with ingot height. Evidently, the fact that the crucible and graphite heating element respectively act as oxygen and carbon sources is a serious problem in mc-Si ingot production. In fact, a study by Raabe et al.[29] suggests that carbon content can be greatly diminished by replacing the graphite heater, whereas the oxygen impurity concentration was directly correlated to the crucible. This has motivated research into replacements such as NBSN crucibles and graphite-free heating elements.

2.2.5 Crystal microstructure

Ingot casting normally takes several days to complete and involves considerable costs in terms of power supply and process supervision. From an economic perspective, it would therefore be desirable to speed up the production and have a high throughput of silicon ingots.

However, as can be seen from equation 2.18, the segregation of impurities is affected by the species' liquid diffusivity D_l and growth rate v. Because diffusion in general is promoted by a temperature increase, increasing the melting rate would also increase ingot diffusion form the crucible and gas flows. Additionally, a large increase in the growth rate implies a large temperature gradient between ingot growth front and melt, which would force impurities to precipitate due to super-cooling. This behaviour has been observed by researches like Trempa *et al.*[30] who documented an increased presence of carbide and nitrate precipitates along grain boundaries at high growth rates. Furthermore, a high growth rate forces silicon to nucleate quickly at the ingot surface. As such the grains have an inclination to form crystal mismatch with the nucleation surface, thereby causing a high degree of crystal defects, grain boundaries and dislocations. A slower growth rate allows larger, vertical grains with low mismatch to grow consistently. Such grains are related to better electrical properties due to fewer grain boundaries, which act as recombination sites.

However, in an effort to compromise between ingot throughput and microstructure it has been conducted studies on sequentially altering growth rate. With this in mind, Arafune *et al.*[31] proposed interrupted growth in which the growth rate is slowed down after a rapid growth stage to allow impurities near the ingot surface to diffuse back into the melt.

.

2.2.6 Growth front

During crystal growth it is imperative to maintain a steady, uniform ingot growth interface. As the shape of the interface determines the amount of stress the grains are subjected to, as well as their size and orientation, it is ultimately the deciding factor for crystal microstructure and stability. In most directional solidification processes, it is ideal to obtain a flat or slightly convex growth interface throughout the entire ingot growth. This can be obtained with an even, vertical heat evacuation down the ingot without any temperature gradients along the growing ingot surface. This also implies that heat flow through the side walls must be minimized, otherwise the columnar grains would begin to nucleate there and adopt a concave growth front and grow diagonally towards the ingot center. Ultimately, the vertically growing grains from the crucible bottom or seed layer would begin to cause mechanical stress on the more diagonally grown grains, thus risking defect formation or fracture. To combat this concave growth front, it has become the new standard to employ adiabatic zones that prevent heat flow through crucible sidewalls. These zones follow the crystal growth front either by suspension or through declination of the crucible itself. With this setup it is possible to obtain a nearly flat growth front.

2.2.7 Melt convection

Melt convection affects ingot microstructure and impurity segregation in the directional solidification of silicon. This is especially true for oxygen and carbon, which are mainly incorporated from the crucible and gas phase, respectively, and have high diffusivity. Because there is no form of stirring in a conventional directional solidification process, most melt flows are weak and are not greatly affected by ingot growth phase but do nevertheless contribute to impurity distribution and grain formation.

Stated somewhat simplistically, melt flows can be separated into two coupled sections: the lower and upper flow vortices. Both vortices are mirrored along the center vertical axis of the ingot and arise due to different but correlating phenomena. The lower vortices area created

from the buoyancy force, otherwise known as natural convection, which is caused by a temperature gradient between the colder region near the ingot growth interface and the upper, warmer region. This temperature difference drives melt flow by slight changes in density. The upper, weaker vortices are smaller and induced by the Marangoni effect, which is a result of a surface tension gradient between the lower vortices and the melt surface.

Initially, natural convection in the lower vortices dominates over the upper Marangoni flows and impurities like carbon are distributed towards the ingot center. However, as the melt volume decreases gradually due to solidification, the temperature difference between the growing ingot and melt-gas interface becomes less pronounced. Near the end of solidification, the Marangoni flows cover most of the melt volume and decouple while moving towards the crucible walls due to surface tension. At this point impurity segregation of species like carbon has progressively moved from the ingot center region and towards the crucible surface.

It should be noted that melt flows can be greatly affected by growth rate and the type of heating installed in the furnace. Nakano *et al.*[32] conducted experiments on directionally solidified silicon ingots where heat was supplied either through side heaters or top heaters. They observed that side heating created a single set of paired vortices, thus annihilating the upper Marangoni vortices. Furthermore, they discovered that oxygen impurities from the silica crucible had decreased due to improved evaporation from the melt surface. As was previously mentioned, Trempa *et al.*[30] attributed carbon and nitrogen precipitation at high growth rates. Their study showed that high growth rates caused poor melt mixing and subsequently poor diffusion of impurities from the growing ingot interface.

3. Experimental method

This section covers the experiments and their methods. Experiments were performed in three stages.

- Testing of silicon wetting properties on both coated and uncoated substrates of oxidized nitride bonded silicon nitride (NBSN).
- Silicon ingot growth in reference crucibles of SiO_2 and consecutive growth in NBSN crucibles.
- Characterization vertical slices taken from grown ingots with respect to impurity content, resistivity and charge carrier lifetime. Gas chromatography was also performed.

3.1. Sessile drop test

The wetting and adhesion properties of solar grade silicon were investigated on two substrates of oxidized NBSN, one of which was not prepared with a surface coating of Si_3N_4. The substrates were produced and provided by Steuler Solar AS represent the same density, porosity and wettability as NBSN crucibles that were used in directional solidification experiments. Prior to the sessile drop test, samples of solar grade silicon were partitioned into pieces of approximately 2.5 mm length before being cleaned in a wet-chemical solution of CP-4 for 20 seconds. The CP-4 solution has a composition of 3 ml HF, 5 ml HNO_3 and 3 ml CH_3COOH. After the chemical cleaning procedure, the silicon pieces were rinsed in deionized (DI) water and dried before being momentarily stored in ethanol.

Only two sessile drop tests were conducted: one on the uncoated Si_3N_4 surface and one on the coated Si_3N_4 surface. The substrates had a cylindrical shape, being 1 cm in width and 0.5 cm in height, in order to fit into a sample stage in the furnace. For each substrate mounting, the substrates were transported with pincers placed across the width to avoid contamination or cracking of the substrate's surface. In the case of the coated substrate, its coated surface was facing upwards. After having mounted the substrate, a single piece of cleaned silicon was placed centrally on top with a pincer. The heating chamber was then closed and vacuumed until the partial pressure of oxygen was $P_{O_2} = 10^{-2}$ mbar with a low-vacuum pump using a custom program interface by SINTEF. The partial pressure was then further reduced around $P_{O_2} = 10^{-2}$ mbar with a high-vacuum pumping system. Following these preparatory vacuuming phases was a series of heating processes under continuous vacuuming, coupled with an

atmosphere of pumped, cleaned argon. Table 3.1 gives a summary of the preset heating configuration used, together with the accompanying oxygen partial pressure range.

Table 3.1: Heating rates for sessile drop test of silicon under vacuum.

Phase #	Heating rate [$^oC/min$]	Target temp. [^oC]	P_{O_2} range $[mbar]$
1	300	1000	$9 * 10^{-12}$ to $6 * 10^{-14}$
2	50	1420	$6 * 10^{-14}$ to $2 * 10^{-17}$
3	5	Until complete melting	$2 * 10^{-17}$ to $1 * 10^{-18}$

The morphology and contact angle of the silicon drop was detected *in situ* by a camera installed level to the substrate stage. Heat supply was cut once the silicon attained a clearly spherical shape above melting temperature, after which the system was slowly cooled to ambient temperature.

3.2. Silicon ingot growth

Prior to ingot growth, cylindrical SiO_2 and NBSN crucibles of electronic grade purity with internal diameter of 25 cm were heated in a heating chamber before being moved with tongs to a revolving stage. The temperature of each crucible is given in table 3.2, together with the names for their respective ingots. The crucibles were not cooled on the stage, which was immediately set to rotate at 2 RPM as they were spray coated with a commercial Si_3N_4 suspension that had been mixed for 24 hours by horizontal ball-milling. The spray coating was performed manually and until an ostensibly even coating was attained. The crucibles were subsequently placed back in the heating chamber with tongs and remained there for drying. Table 3.2 gives the drying temperature for each crucible.

Table 3.2: Ingot name and crucible types.

Ingot name	Crucible material	Coating temp. ^oC
IC4	SiO_2	1100
IC5	SiO_2	1100
IC6	NBSN	1250

IC7	NBSN	1100

Preparatory measures in the form of nitrile gloves, hair net, lab coat and filter breathing masks were taken prior to silicon charge loading in a clean room. Before loading the crucibles with pieces of solar grade silicon, the crucibles were placed in insulating graphite casks after which a 2-3 cm thick seeding layer of finely grained silicon of the same quality was placed in the crucible bottom. Once the desired charge was loaded, the boron ($k_0 = 0.78$) dopant quantity was added to the top as a powder. A summary of the ingredients used in each ingot is given in table 3.3, where the desired resistivity at the seeding layer was calculated by using the ASTM F723-99 empirical standard for determination of resistivity in p-type silicon based on N number of acceptor atoms added. It is given as the following equation.

$$\rho = \frac{1.305 \cdot 10^{16}}{N} + \frac{1.133 \cdot 10^{17}}{N\left[1 + \left(2.58 \cdot 10^{-19} N\right)^{-0.737}\right]} \qquad (3.1)$$

It is important to note that IC4 and IC5 used individual crucibles that were discarded after solidification, whereas IC7 was solidified in the cleaned and recoated crucible from IC6. The loaded crucible and graphite insulation was then carefully transported to the Crystalox DC250 directional solidification furnace.

Table 3.3: Overview of ingots and their ingredients. Total weight includes seeding layer.

Ingot name	Dopant charge $[g]$	Total wt. Si $[kg]$	Si seed $[kg]$	Resistivity $[\Omega cm]$
IC4	3.4	16	4	4.4077
IC5	16	16.7	4	1.0212
IC6	16	16.7	4	1.0212
IC7	16	16.7	4	1.0212

The furnace was then closed and pumped to vacuum before starting argon venting and finally heating. The temperature profile for each ingot were slightly different with respect to heating rate, but they all used the same holding temperatures. The temperature profile for each ingot can be seen in figures 3.1 to 3.4. However, each load was melted so that the seeding layer was left intact. A gas chromatography system was also implemented in order to detect evaporate gases from the melt phase.

In figure 3.1 to 3.4, each plot gives a series of temperatures detected in certain areas of the ingots. “Heater TC1” is the temperature measured at the top of the silicon load by

thermocouple 1 and indicates the highest temperature that the load is subjected to by heating. The desired temperature is adjusted automatically depending on the detected values from thermocouple 1. The calculated heating is supplied by the upper heating element and denoted "Working SP". Similarly, thermocouple 2 detects the temperature at the bottom of the crucible, which is denominated "Pedestal temperature" in the figures. In order to initiate crystal growth, the melt must be cooled from the bottom up using a cooling system for vertical heat leak (VHL). This is done by convective heat transfer to water flowing in pipes underneath the crucible, whose flow rate is automatically regulated to attain the calculated temperature denominated as "VHL" in the figures. This convective heat transfer is used in conjunction with argon gas flow. As can be seen for all temperature profiles, the VHL system commences when the entire silicon load is melted and the detected temperatures from thermocouples 1 and 2 are stabilized. It should be noted that vertical translation for all processes begins from the top of the 2-3 cm thick seeding layer, and in the case of IC4 it is given as a percentage of the total ingot height.

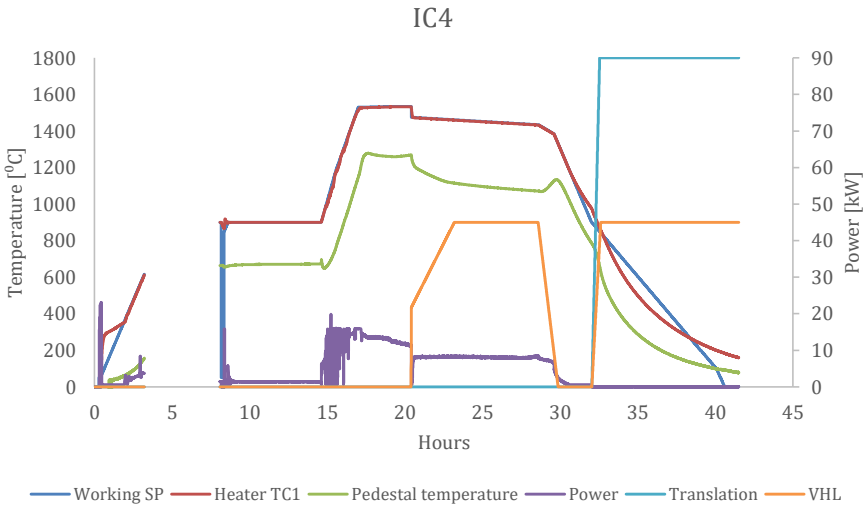

Figure 3.1: Temperature profile from the automated growth of ingot IC4.

As can be seen in figure 3.1, the temperature profile of ingot IC4, which was produced in a SiO_2 crucible, displayed irregularities prior to the 5-hour mark. Initially, heating commenced with a large power spike to approximately 22 kW, which caused a strong temperature increase at the top of the load. Thermocouple 2 only detected a minor increase in

temperature at the crucible bottom as most of the heat was dispersed throughout the upper region. After 600 ^{0}C was reached at the top, neither the thermocouples nor the power supply was logged until 880 ^{0}C was reached.

Despite this discrepancy the process had proceeded as planned, and was at this point followed by a holding stage for approximately 6 hours. At this stage the system was allowed to a reach steady state of 900 ^{0}C at the top and 650 ^{0}C at the seeding layer, prior to commencing the melting stage. By increasing the power output to the heating element, the temperature was steadily raised to 1530 ^{0}C at the top, which is well above the 1414 ^{0}C silicon melting temperature. In order to preserve the seeding layer, the temperature was modulated to 1271 ^{0}C at this crucible height. After holding these temperatures for about 3 hours, the silicon charge was completely melted down to the seeding layer.

At this point the VHL system was primed and commenced to create a temperature gradient between the solid seeding layer and the melt, thus causing ingot growth. At first the flow rate increased steadily for the first 3 hours in order to let the ingot quickly grow past the seeding layer, but was then stabilized to allow constant growth rate for 5 hours. When thermocouple 1 detected that the temperature above the ingot had decreased to below melting point, the VHL was switched off and the solidifying ingot was allowed to cool down unaided to approximately 900 ^{0}C. At this point the ingot was lowered away from the heating element while undergoing VHL cooling to room temperature.

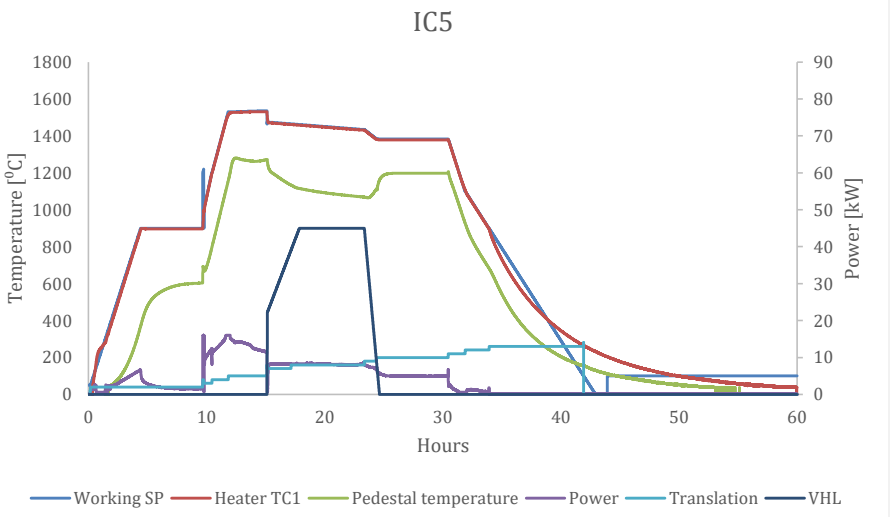

Figure 3.2: Temperature profile from the automated growth of ingot IC5.

IC5 was produced similarly to IC4 with a few alterations to the processing steps. Firstly, vertical translation started form the seeding layer, right after the first holding stage at 900 ^{0}C, and proceeded incrementally throughout the whole process. It is also worth mentioning that the holding temperature at the seeding layer was near 600 ^{0}C rather than 670 ^{0}C, as it was for IC4. Secondly, after the ingot had been completely solidified following 25 hours of operating time, it was annealed for 5 hours. The VHL system was switched off at this point, so the temperature decreased unaided from 1378 ^{0}C at the ingot top thermocouple and increased to 1169 ^{0}C at the bottom thermocouple. Thirdly, after the heating was switched off, the ingot was allowed to cool to room temperature while still undergoing vertical translation.

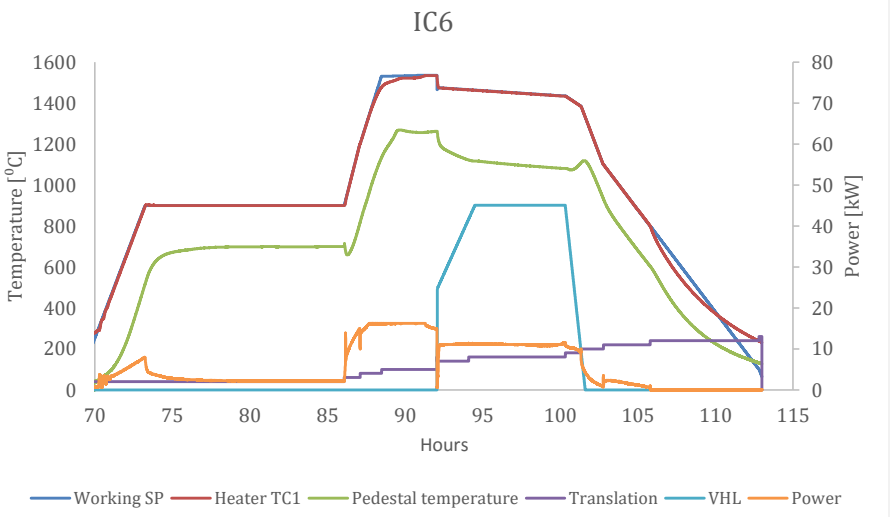

Figure 3.3: Temperature profile for the automated growth of ingot IC6.

IC6, which was solidified in a Si_3N_4 crucible, also had a temperature profile that distinguished itself slightly from those of IC4 and IC5. First of all, its pre-melting holding stage was 13 hours long rather than 6 hours for IC4 and 5 hours for IC5., This had no practical cause and only occurred due to a delay.

As for the melting stage, it was performed at the same relative temperatures as IC4 and IC5, and the solidification was performed at an identical rate as the proceeding experiments. However, a slight deviation from IC4 and IC5 is notable at the melting stage after 88 processing hours where the susceptor needs more time to reach the target temperature of "Working SP". This is due to the higher thermal conductivity of the Si_3N_4 crucible, which causes more heat to be evacuated during the melting stage, compared with IC4 and IC5 temperature profiles.

The vertical translation was incremental throughout the process, as it was for IC5. There was no annealing stage after solidification, and the unaided cooling to room temperature was slightly longer than for IC4 and IC5.

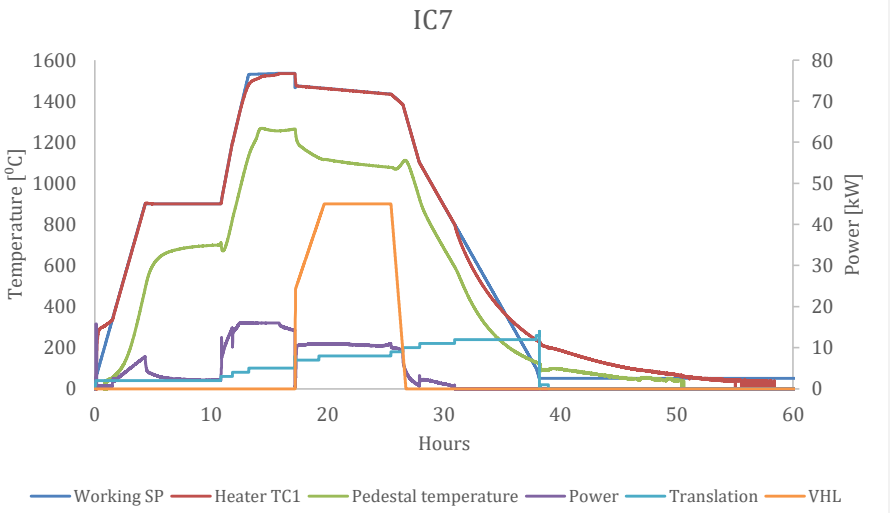

Figure 3.4: Temperature profile for the automated growth of ingot IC7.

The temperature profile of IC7 is similar to that of IC6. As there was less or no delay prior to melting, the holding time was considerably shorter. Melting of IC7 also took longer compared with IC4 and IC5, due to the higher thermal conductivity. Like for IC6, there was no annealing for IC7 after solidification and cooldown was performed at an equal rate.

After a successful solidification process, each ingot was sectioned by the company Steuler-KCH according to figure 3.4 by diamond wire sawing with a SiC slurry.

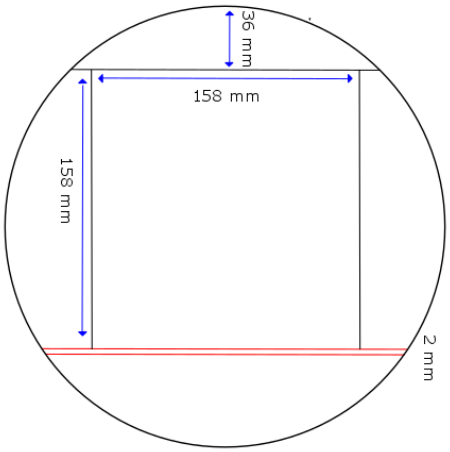

Figure 3.5: Horizontal cross section of a grown ingot and its cutting schematics. The red lines signify the 2 mm vertically cut slice that was investigated per ingot.

For each ingot, the area of interest in this thesis was the vertical slice that borders on the square central region, as can be seen in the cutting schematic. As the square center region is outside of the "red zone" of the ingot where diffusion from the crucible has contaminated the silicon, it is of high purity and can be processed into wafers. The vertical, 2 mm slices are taken sufficiently close to the center region to allow comparative analysis of the ingot. After sampling from the ingots, each 2 mm slice aside from IC7 was cut in half to reduce the surface area. By symmetrically halving the surface area to be investigated, the raster scan time could be reduced.

. The ingots' conductive properties were mapped with µPCD raster scans, their resistivity was investigated with the four-point probe (FPP) method and their impurity content of O_i and C_s as a function of ingot height was measured with FTIR. In addition, the gas chromatography for each ingot was analyzed with respect to temperature and process stages.

3.3. Characterization

This chapter presents the equipment and methods used to characterize samples from IC4 to IC7. Prior to performing measurements, the samples were abrasively grinded and then polished. Measurements were performed with a µPCD system, with FTIR spectrometry and with FPP to determine the samples' carrier lifetime, impurity concentration and resistivity, respectively.

3.3.1. Sample polishing

Sectioned samples were wax-mounted onto rotator sample holders and smoothened with a Struers Pedemax-2 by water abrasive grinding with SiC paper. The grinding sequences used can be seen in table 3.3.

Table 3.4: Sample grinding plan. Grit size signifies the number of SiC granules on the paper per square inch.

Sequence #	Grit size	Rotation speed $[RPM]$	Duration $[min]$
1	P320	100	4
2	P500	100	4
3	P1200	100	3
4	P2000	100	3

After grinding a sample at a certain grit size, it was rinsed in running water to remove debris and grains that could otherwise scar its surface. After grinding down sample surfaces with P2000 SiC paper, they underwent automated polishing with a diamond slurry and microfiber polishing cloth in a Struers AbraPol-20 polishing machine. Also this time the sample's surface was cleaned in water after each sequence to reduce the likelihood of scratches. The polishing plan is given in table 3.4.

Table 3.5: Sample polishing plan. The grain size signifies the diameter of diamond particles in the suspension, whereas the polishing cloths are classified according to fiber thickness.

Seq. #	Lubricated	Suspension	Grain size $[\mu m]$	Cloth	Duration $[min]$
1	Yes	Struers DP P	9	9 µm MD-Mol	3
2	No	DiaPro M	3	3 µm DP-Mol	3
3	No	DiaPro Nap B	1	1 µm DP-Nap	3

After surface polish the samples were water rinsed, then detached from the sample holder using hot water and finally cleaned with ethanol.

3.3.2. Microwave photoconductive decay (μPCD)

A SEMILAB WT-2000PVN μPCD system was used to obtain charge carrier lifetime and differential resistivity maps. The former is measured by local, burst injection of microwaves into the conducting samples surface, at which point the concentration of excited minority charge carriers will increase greatly. The excited charge carriers will eventually recombine with any opposing charge carriers, defects or impurities. Upon conducting recombination, the excess energy will be reemitted as longer wavelength photons, which are detected by the system. The photoconductive decay method thus gives an indication of the local lifetime in a conductive material, and by extension an overview of impurity and defect distributions in the sample.

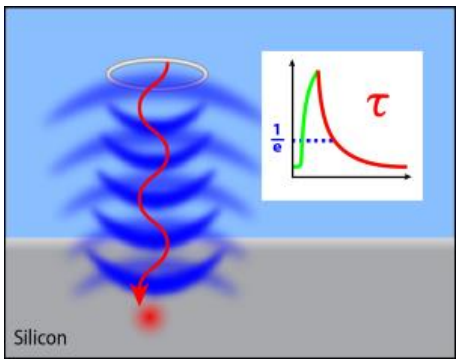

Figure 3.6: Photoconductive decay in silicon.

Conductivity and thereby resistivity is mapped with the same equipment by employing magnetic fields oscillating at radio frequency (RF)[33]. The magnetic field from an emitter induces two paired sets of closed current loops in the sample's surface. One closed circuit is caused by the magnetic field entering the sample surface, thus inducing an electric field perpendicular to the magnetic flux according to Faraday's law of induction. The other electric field is caused by the magnetic flux exiting the sample surface. The right hand rule states that an electric field induced from a magnetic field will have anticlockwise and perpendicular motion relative to the magnetic field. Thus each closed electric field has equal magnitude as one another, but experience opposing spin. Furthermore, because electrons have a negative charge, their motion is opposite to the induced electric field. As stated by Lenz's law, a closed electric current will establish its own magnetic field whose direction is determined by the right hand rule. The end result is that the two induced current loops create paired, but opposing

magnetic fields. The magnetic field pointing towards the inducing magnet exerts a repulsive force, whereas the other magnetic field reinforces the original magnets field and therefore exerts and attractive force. The creation of these paired magnetic fields causes a drag force that locks the magnet and sample in place. The kinetic energy necessary to overcome this drag is dependent on the magnitude of the material's conductivity, because it determines the strength of the Lenz-induced magnetic fields. Thus the induced eddy currents can be used to determine conductivity locally on a sample's surface.

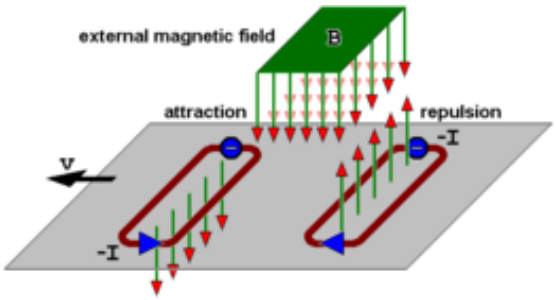

Figure 3.7: The principle of eddy currents created by induction from an external magnetic field.

Samples were mounted on the scanning platform and their geometry outline was detected by the accompanying software's optic or microwave 5-point scan modes. IC4 and IC4 were raster scanned in the dark at 500 µm resolution, whereas IC6 and IC7 were raster scanned at 250 µm resolution. Both minority carrier lifetime and resistivity was mapped for all samples.

3.3.3. Fourier transform infrared spectrometry (FTIR)

FTIR is spectrometric technique that allows for characterization of materials and analysis of their composition. In FTIR spectrometry a monochromatic laser beam, whose wavelength lies somewhere in the IR spectrum, is transmitted through a sample. Using a movable beam splitter and interference between transmitted light, the recombined light's wavelength can be adjusted. This makes it possible to create several wavelengths simultaneously. Certain materials, like silicon, are transparent at IR wavelengths but may contain impurities whose chemical bonds resonate at these frequencies. This is the case for O_i and C_s, whose chemical bonds Si-O-Si and Si-C in the crystal lattice vibrate at frequencies 1107 cm^{-1} and 605 cm^{-1}, respectively. Some of the transmitted light at these frequencies will be absorbed by the contaminants, thus allowing identification by using Beer-Lambert's law:

$$A = abc \qquad (3.2)$$

Where A is the measured absorbance, a is the chemical bond's absorptivity, b is the sample thickness and c is the impurity concentration. Because the other variables are detected simultaneously, only the concentration is unknown.

In this thesis the concentrations of O_i and C_s were measured with FTIR spectrometry as a function of ingot height, including the seeding layer and with a 5 mm interval between data points. The spectra were manually collected from the sample's central region with the OMNIC FTIR spectrometry software developed by Thermo Scientific. Prior to performing spectrometry on a new ingot sample, the background spectrum was collected. The interstitial oxygen calibration coefficient was preset to 6.28.

3.3.4. Four-point probe (FPP)

The 4PP method is a simple and much used technique for measuring sheet resistivity in semiconductors. The apparatus consists of four probes with mutually equal spacing S, where a current passes from the outer probes and through the sample surface due to their low resistance. The inner probes, however, have a comparatively high resistance and therefore can be used to measure the voltage between the outer probes. The apparatus schematic can be seen in figure 3.7.

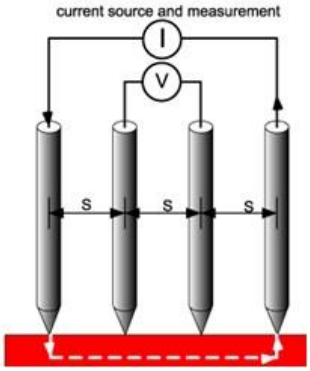

Figure 3.8: The FPP setup.

The current strength is predetermined and controlled by the power source, whereas the measured voltage will fluctuate depending on the local resistivity. Resistivity in mc-Si increases predominantly in the presence of grain boundaries, impurities or other defects.

Voltage measurements were performed centrally on samples along their entire height, starting from the bottom. The voltage at each data point was calculated as an average of reverse and forward current with accompanying standard deviation, and the probe of choice had a spacing s = 1,591 mm. Measurements in IC7 was conducted in three columns with a 2 cm horizontal spacing. Measurements from the other samples were only done in two columns as they were already cut, but their column spacing was also 2 cm. The vertical interval between each measurement point was 0,5 cm.

Resistivity ρ was then calculated for each data point using the following equation

$$\rho = 2\pi s \frac{V}{I} \qquad (3.3)$$

In which V is the measured voltage in mV and I is the average current in mA.

4. Results

This section presents the results obtained in the thesis by the sessile drop method, FPP, FTIR and µPCD. Scheil plots were also created from resistivity measurements from FPP to give a graphic comparison between predicted and measured values. As was mentioned in section 2.2.3, the Scheil model is used to graph impurity concentrations with respect to solidification fraction f_S. Because resistivity in p-type silicon correlates inversely to the dopant concentration, the Scheil model can be used to investigate how well the dopant is dispersed in the ingot.

4.1. Contact angle

This section covers the results obtained from the sessile drop experiments of silicon on Si_3N_4 substrates, both uncoated and coated with Si_3N_4. It should be clarified that automatic goniometer was implemented in the apparatus. Therefore, the contact angle θ_C for silicon on both coated and uncoated substrates of Si_3N_4 was determined visually by using an image editing program on the photographs taken by the built-in camera in the apparatus. Photographs were

taken continuously during both experiments, but only the last images were chosen for investigation of the angles.

4.1.1 Uncoated Si_3N_4 substrate

The sessile drop of silicon on uncoated Si_3N_4 is shown in figure 4.1. The puddle of silicon surrounding the solidified droplet was caused as the solid sample melted inwards.

Figure 4.1: Photo of a sessile drop on uncoated Si_3N_4 sample substrate.

Substrate surface was uncoated and therefore initially expected to be slightly wet by liquid silicon. An observable feature was the partial reduction of drop volume without affecting its shape or contact angle.

Past melting temperature, the holding stage appeared to slightly vibrate and displace the now liquid droplet towards one of the substrate edges.

An interesting feature of the silicon that covers the substrate is the fact that it covers such as large area. In other words, the silicon was not withheld by capillary forces from pores but rather appears to only cover the outer porosity of the substrate.

Figure 4.2 depicts the recently solidified silicon droplet after the experiment was terminated. The artifact or “hat” covering the droplet grew quickly as the droplet solidified inwards. Although the silicon had slightly smeared the droplet foundation and made the contact angle difficult to discern, it was determined to be approximately 106^0 on the left side and 97^0 on the right side.

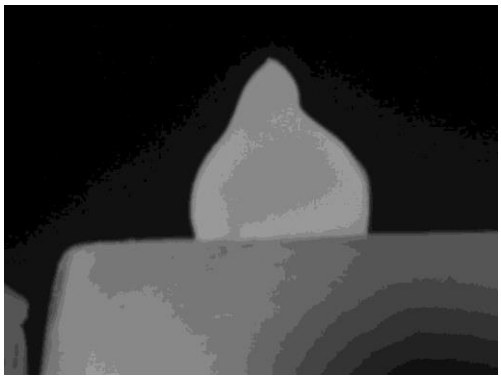

Figure 4.2: Sessile drop on an uncoated Si_3N_4 sample substrate. The left angle is 106^0 and the right angle is 97^0.

4.1.2 Coated Si_3N_4 substrate

Figure 4.3 shows the result of a sessile drop test on a Si_3N_4 substrate coated with Si_3N_4. The formation sequence was identical to the previous sample: radial melting of the solid silicon, partial collapse and then reformation into a droplet. However, compared to the sessile drop test on the uncoated substrate, this coated substrate displays considerably less smearing from the molten silicon.

Figure 4.3: Photo of a sessile drop on coated Si_3N_4 sample substrate.

The smeared silicon covers substantially less substrate surface area and in lesser quantity compared to the preceding experiment. Visual inspection of the smear suggests that the liquid phase has only succeeded in covering the very exterior of the coating. There was no visible collapse or reduction of drop volume during the test, nor did the contact angle change

after complete liquefaction of the silicon. No noticeable vibration was detected during or after liquefaction of the silicon.

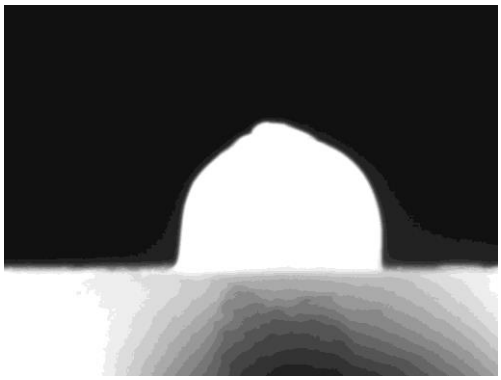

Figure 4.4: Sessile drop on a coated Si_3N_4 sample substrate. The left angle is 87^0 and the right angle is 93^0.

Figure 4.4 shows the solidified, sessile drop of silicon on the coated surface as taken by the apparatus. Unlike the other droplet, it this one only achieved a lesser artefact or hat. As was expected from the lack of smearing on the substrate surface, the droplet base was more well defined. Therefore, the contact angles of the droplet's left and right side could be measured as 87^0 and 93^0, respectively.

4.2. FPP

This section presents ingot resistivity measured by FPP and as a function ingot height, starting from the bottom. Ingot height is given as a fraction of the total height, thus making the resistivity at a given point more comparable to that of other ingots. It should be noted that each data point is a mean value of resistivity calculated from measurements of forward and reverse currents through the FPP probes. In other words, the magnitude of standard deviation for each data point in the figures shown are a result of comparability between the forward and reserve currents. All ingots display a larger standard deviation at lower fraction height due to inaccuracies in current measurements in these regions. These discrepancies can be explained by the fact that forward and reverse current measurements by FPP may yield different values if the probe spacing is larger than the grain size. Consequently, the currents differ if the they cross one or several grain boundaries at this point. The grain size is smallest near or in the seeding

layer and increases sharply with ingot height, which also explains why the decrease in resistivity standard deviation follows the same trend.

The coloring of each resistivity plot is not arbitrary. Plots for IC4, IC5 and IC6 with red curves are from measurements taken 0,5 cm from the ingot center axis. These samples are half cross sections, thus measurements were taken slightly removed from the edge to prevent current shunting and erroneous measurements. The red curve in figure 4.15 for IC7 is taken from the center axis because IC7 was a complete cross section of the ingot, thus current shunting was not an issue.

Blue resistivity curves are from measurements taken 2 cm from the center (red) measurement line, thus 2,5 cm from the ingot center axis. As samples IC4, IC5 and IC6 are half cross sections from their respective ingot, they had only room for one blue measurement each. Because IC7 was larger, it had two “blue” lines mirrored 2 cm from the center axis.

Finally, the green resistivity curve for each sample is constructed from the mean values of center and off-axis lines.

4.2.1 IC4

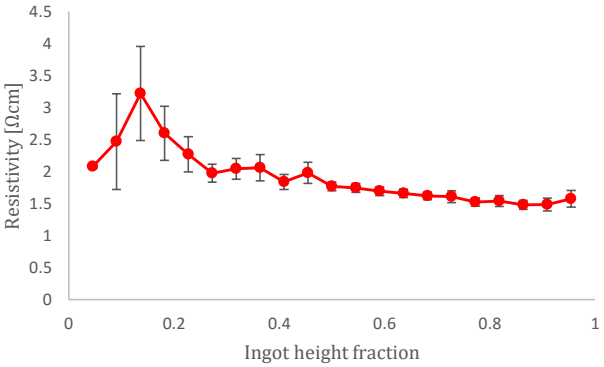

Figure 4.5: Resistivity as a function of IC4 ingot height, taken 0.5 cm from the center axis.

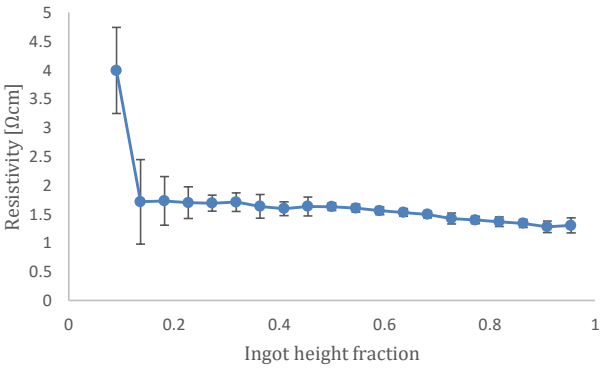

Figure 4.6: Resistivity as a function of IC4 ingot height, taken 2.5 cm from the center axis.

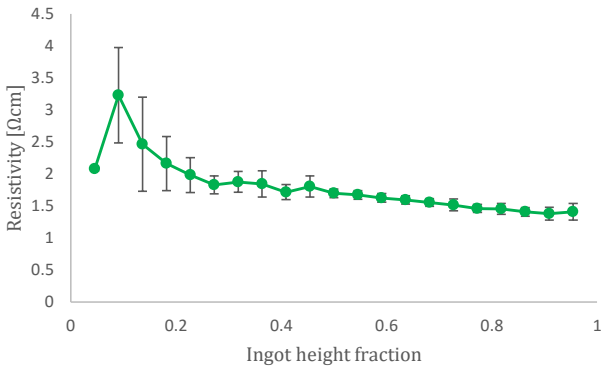

Figure 4.7: Mean resistivity as a function of IC4 ingot height.

4.2.2 IC5

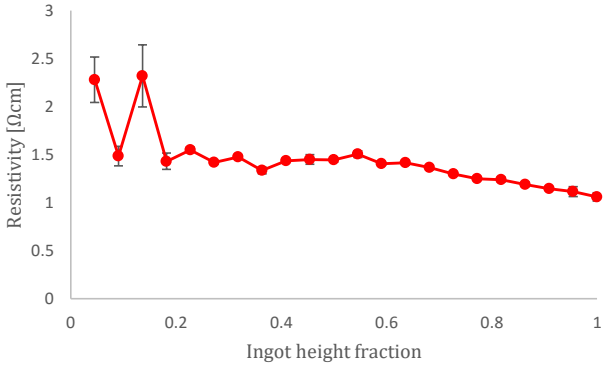

Figure 4.8: Resistivity as a function of IC5 ingot height, taken 0.5 cm from the center axis.

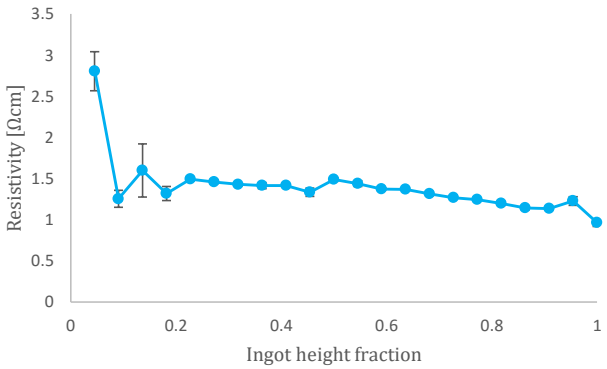

Figure 4.9: Resistivity as a function of IC4 ingot height, taken 2.5 cm from the center axis.

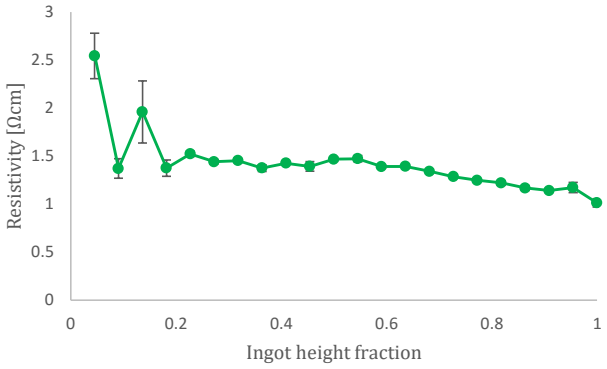

Figure 4.10: Mean resistivity as a function of IC5 ingot height.

4.2.3 IC6

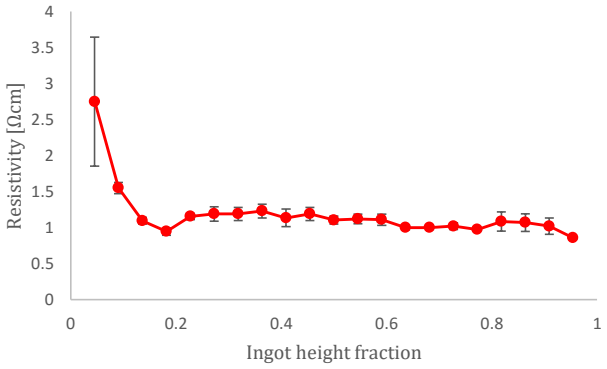

Figure 4.11: Resistivity as a function of IC6 ingot height, taken 0.5 cm from the center axis.

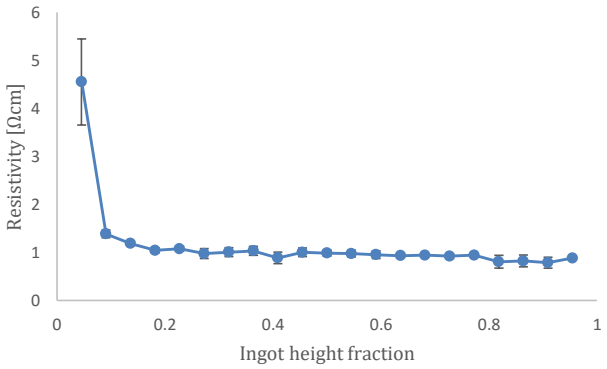

Figure 4.12: Resistivity as a function of IC6 ingot height, taken 2.5 cm from the center axis.

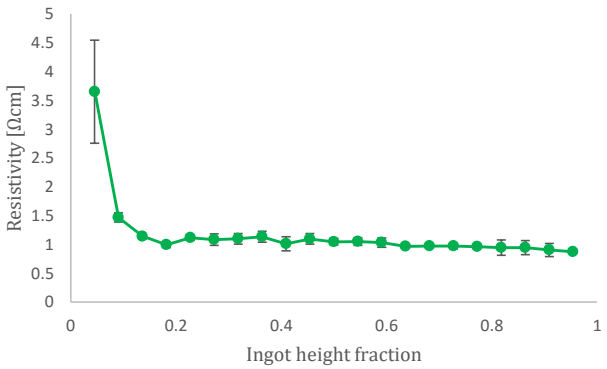

Figure 4.13: Mean resistivity as a function of IC6 ingot height.

4.2.4 IC7

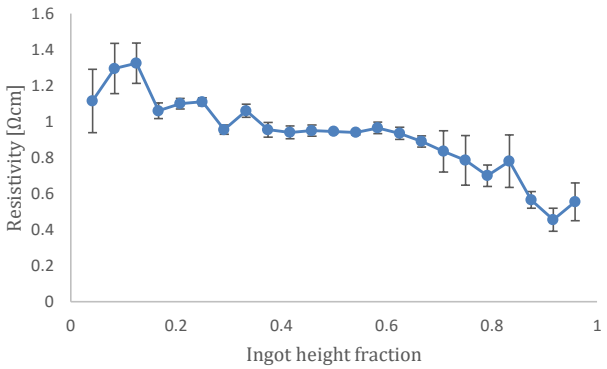

Figure 4.14: Resistivity as a function of IC7 ingot height, taken 2 cm left of the center axis.

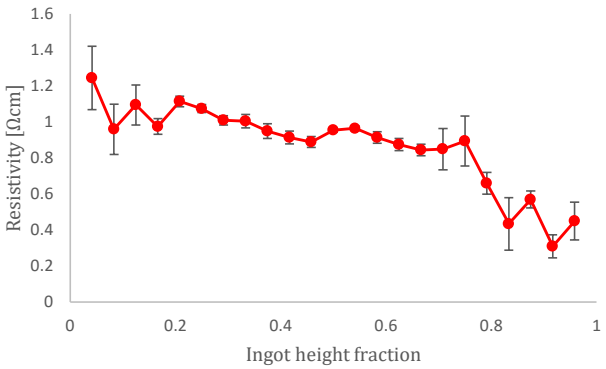

Figure 4.15: Resistivity as a function of IC7 ingot height, taken from the center axis.

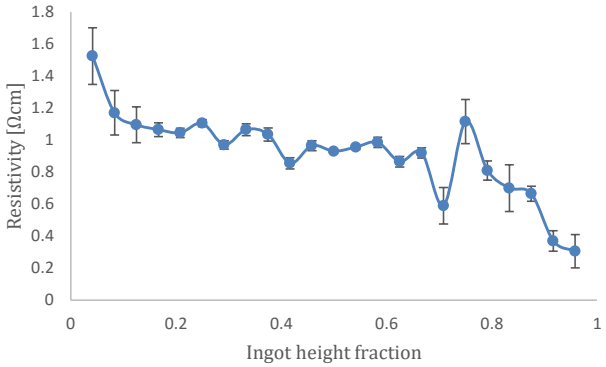

Figure 4.16: Resistivity as a function of IC7 ingot height, taken 2 cm right of the center axis.

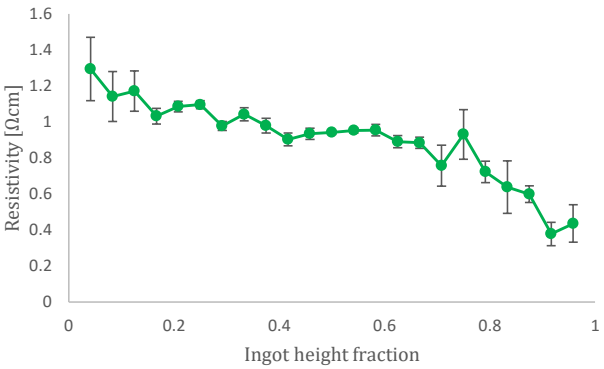

Figure 4.17: Mean resistivity as a function of IC7 ingot height.

4.2.5 Combined resistivity plot

The plots in figure 4.18 are a compilation of the mean resistivity plots from IC4 to IC7, as shown in figures 4.7, 4.10, 4.13 and 4.7. For the sake of readability, the standard deviations were not included in the compilation.

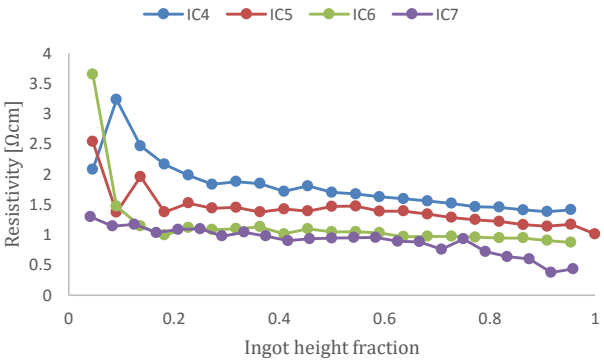

Figure 4.18: Mean resistivity for ingots IC4, IC5, IC6 and IC7 as a function of ingot height.

As shown in the figure, the resistivity for the ingots IC4 and IC5, which were cast in silica crucibles, is considerably higher than IC6 and IC7. The exception is the seeding layer in IC6, which was cast in a silicon nitride crucible, where the resistivity increases sharply compared to the others. Another interesting feature is the fact that IC7, which was cast in the

silicon nitride crucible reused after IC6, exhibits the lowest and most uniform resistivity of all the ingots regardless of height fraction.

4.3. FTIR

This section presents the FTIR measurements performed in this thesis. The aim and motivation for using FTIR was to investigate the concentrations of interstitial oxygen O_i and substitutional carbon impurities C_s as a function of ingot height. Background spectra were collected prior to commencing on a new sample and calibration coefficient for O_i was set to 6.28. Only single measurements were conducted per data point, thus standard deviations for each sample was not constructed.

4.3.1 Interstitial oxygen concentration

The O_i concentration profiles of each sample is shown in figure 4.19. The concentration is high at the seeding layer and decreases with ingot height. This behaviour is well known due to oxygen's k_0 coefficient being 1.25, which is does not adhere well to the Scheil model as it is higher than unity. By referring to table 2.1 and equation 2.13, it is therefore apparent that oxygen prefers to segregate into the solid phase. Interestingly, the concentration profiles in the figure are comparable to the resistivity measurements done with the FPP method, shown in figure 4.18.

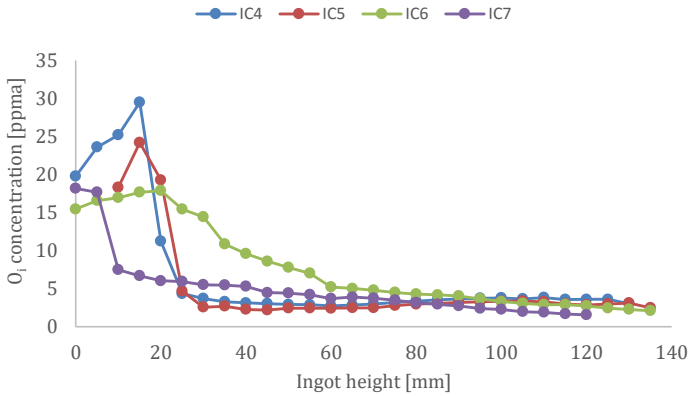

Figure 4.19: O_i concentration for each ingot as a function of its height.

IC4 and IC5, which were cast in coated SiO_2 crucibles, are expected to display greater oxygen contamination than IC6 and IC7 due to the crucible's composition. Oxygen concentration should be higher in IC4 and IC5 because it diffuses from the crucible during processing. However, there are three points of interest worth remarking:

1. O_i concentration in IC6 is quite high and equal to IC7 at the very beginning of the seeding layer.
2. In IC6, the O_i concentration decreases more gradually than for any of the other ingots.
3. The O_i concentration in IC7, which is the ingot made in the reused Si_3N_4 crucible, appears to be more restricted to the seeding layer. Overall, less oxygen has diffused into the IC7 ingot during the process

4.3.2 Substitutional carbon concentration

The C_s concentration profile for all the ingots is shown in figure 4.20. By referring to table 2.1 and equation 2.13, the concentration profiles seem to agree with the Scheil model. The k_0 coefficient for carbon in silicon is only 0.07, therefore carbon is expected to segregate into the melt to a much greater extent than oxygen. This means that incorporation of carbon into the ingot is expected to be diminutive in the initial solidification and increase steadily as the melt concentration increases.

However, as is shown in figure 4.20, the carbon concentration deviates from the model on three observable accounts.

1. The carbon concentration is raised in the seeding layer, before decreasing to a lower value at the interface between ingot and the seeding layer.
2. Carbon is not a natural ingredient of the crucible composition in either crucible type, and as such its concentration was not expected to decrease from reuse of the NBSN crucible. In fact, its concentration was expected to be comparable in each ingot type, as shown in figure 4.20. However, the carbon concentrations in IC6 and IC7 are surprisingly found to be much higher throughout the ingot, compared to the profiles for IC4 and IC5.
3. In addition, the carbon concentration only seems to accurately follow the Scheil model in the case of IC6 and IC7. Disregarding the concentration discrepancies in the seeding layer, these concentration profiles increase steadily with ingot height, as the model predicts. However, IC4 and IC5 profiles remain relatively stable until about 85 mm ingot height, at which point both profiles begin to increase exponentially.

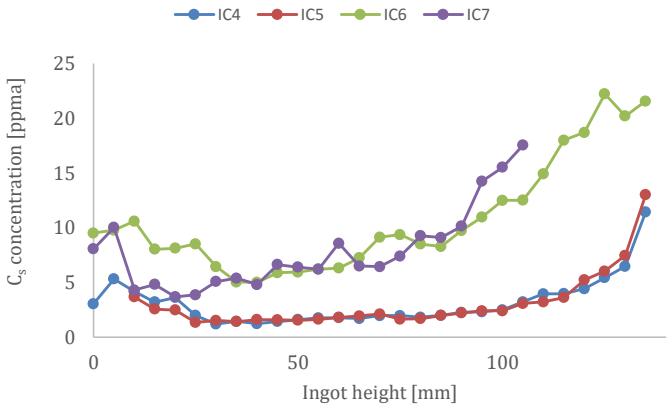

Figure 4.20: C_s concentration for each ingot as a function of its height.

4.4. Lifetime and resistivity mapping

This section presents the lifetime and resistivity mapping of samples IC4 to IC7, which was performed by µPCD and eddy current raster scans, respectively. IC4 and IC5 were raster scanned with 500 µm resolution, whereas both IC6 and IC7 where scanned with 250

µm resolution. In the case of µPCD mapping, resolution is defined as the spacing between each scan point.

As shown in the following lifetime maps, each ingot was grown on a seeding layer at the crucible's bottom. This is depicted as a densely packed, red layer on which grains grow vertically to obtain low mismatch and thermal strain with adjacent grains. The seeding layer, and parts of the ingots that are in immediate contact with the crucible, all exhibit low carrier lifetimes due to thermal strain and diffusion of impurities from the crucible. These regions are called "red zones". Because diffusion of impurities, defects and thermal strain is a function of ingot growth rate and temperature, these parameters will affect the shape of the inner zone where carrier lifetime is expected to be higher. During fabrication of mc-Si solar cells, only this "blue zone" can be extracted and processed further. As such it is imperative to maintain high lifetimes in this region of the ingot and, if possible, ensure that it is free of defects and impurities like transition metals, O_i and C_s. Preferably, it should also have a cubic morphology to ensure that loss of silicon is minimized.

µPCD carrier lifetime mapping is not only useful for defining carrier lifetime zones, but also for attaining a better understanding of the ingot's crystallinity and distribution of impurities. Impurities tend to accumulate at preferential like at grain boundaries or defects, where they diminish carrier lifetime by trap-assisted recombination. Consequently, carrier lifetime maps constructed by µPCD can be used to obtain a qualitative understanding of the grain size, their orientation and impurity contamination of the ingot.

In the following figures, the outline of some grain boundaries may be discerned as green, yellow even red areas depending on carrier lifetime. The size of these areas are affected by defect density; higher defect density means larger outlines.

Accompanying each carrier lifetime map is a resistivity map constructed using eddy currents. As is shown in the scans and was predicted by the Scheil model for boron doping of silicon, the resistivity decreases with ingot height. More interestingly, because resistivity in silicon is so dependent on dopant concentration it can be used to qualitatively investigate how and where a dopant has segregated during the course of solidification.

4.4.1 IC4

The lifetime map of IC4 in figure 4.21 shows well-defined red and blue zones. The red zone is prominent near the seeding layer, as expected, but does not cover much area laterally from the crucible-ingot interface. Another interesting feature in this region is the higher lifetimes, as depicted by an orange hue.

The blue zone is regular and cubic near the seeding layer, but has expanded more towards the crucible sidewalls during ingot growth. Lower carrier lifetime can be observed along certain grain boundaries in the blue zone as yellow lines, but they do not extent into the blue zone to an appreciable extent. The yellow or green boundary between the red and blue zones, which has intermediate carrier lifetimes, is thin and defined.

Some irregularities in the form of low lifetime regions penetrate into the blue zone, as seen in the upper left corner of figure 4.21. Another is the large sliver near the center axis.

Carrier lifetime in the blue zone is at most 7.651 µs, but averages at approximately 7 µs.

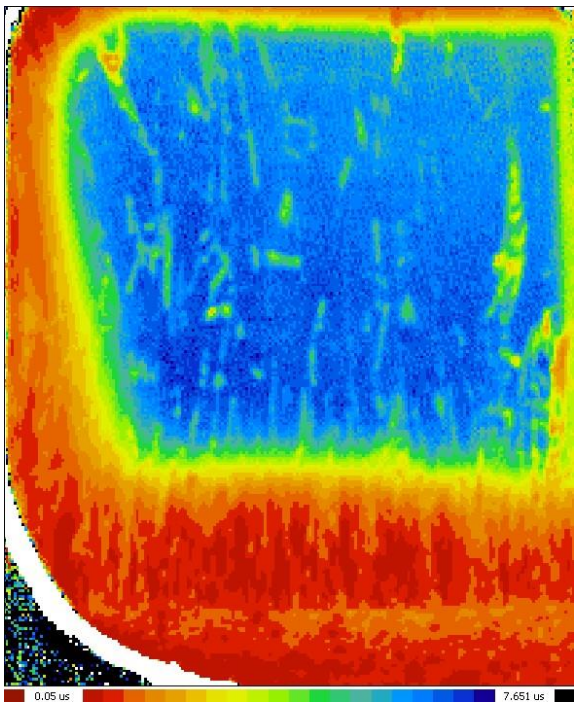

Figure 4.21: Mapping of carrier lifetime in IC4 by µPCD.

The resistivity map of IC4 is shown in figure 4.22. The resistivity decreases with ingot height, as expected from FPP measurements. However, the FPP measurements do not account for the migration of low resistivity zones towards the crucible sidewall as the ingot approaches complete solidification, as shown in the current figure. At the very end of solidification, the resistivity has decreased to 2.113 Ωcm from 4.843 Ωcm at the very bottom of the sample. However, it should be noted that the sample edges increase resistivity by causing shunting during eddy current measurements. A more accurate representation of resistivity near the edges would be the adjacent zones.

Figure 4.22: Mapping of resistivity in IC4 by eddy currents.

4.4.2 IC5

The carrier lifetime map of IC5 is shown in figure 4.23. By studying the figure, it becomes clear that IC5 distinguishes itself from IC4, although they were grown in the same crucible type. First of all, the red zone dominates more of the ingot volume, especially in the upper region. Secondly, the presence of defects and impurities appears to be more pronounced. This is shown as yellow outlines in the blue zone, which appear more densely and larger than in IC4. These tendrils of lower carrier lifetime invade the blue region primarily from the bottom of the crucible, but a single strand protrudes from the upper red zone. Thirdly, the boundary between the red and blue zone is thicker and less clearly defined. Some of it also extends towards the crucible wall.

Despite these differences the carrier lifetime is on par with IC4. The lifetime in the red zone is actually slightly higher than it is in IC4.

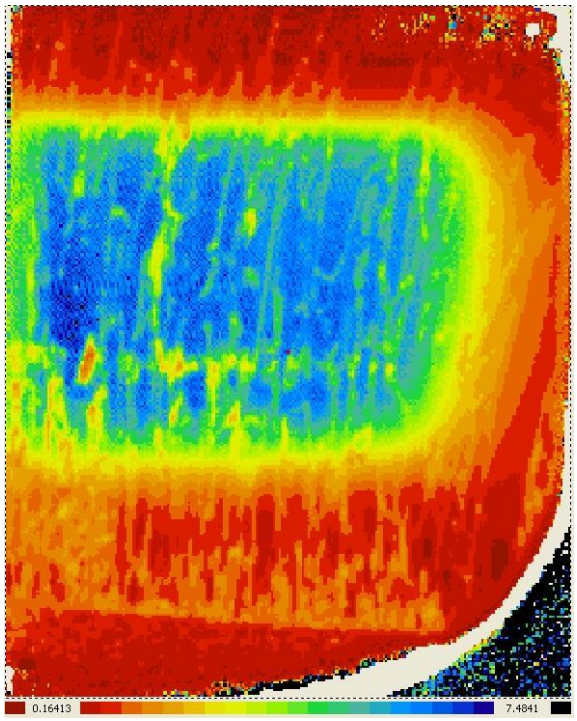

Figure 4.23: Mapping of carrier lifetime in IC5 by µPCD.

The resistivity map for IC5 is shown in figure 4.24 and resembles the one for IC4. Lifetime decreases with ingot height and towards the crucible sidewall. A notable difference is the size and distribution of the lower lifetime zones in the upper ingot region. At the upper ingot region, the resistivity zones are arranged in layers that stretch all the way to the ingot center. The area with the lowest resistivity is triangular and stretching towards the ingot center. This is in contrast with resistivity zones in IC4, where they have a more radial distribution from the upper left side.

Another notable feature is that resistivity in IC5 as a whole is lower than in IC4. Even when accounting for the shunting effect on the edges, the resistivity is at most 3.8364 Ωcm and approaches 1.8965 Ωcm at the upper right area.

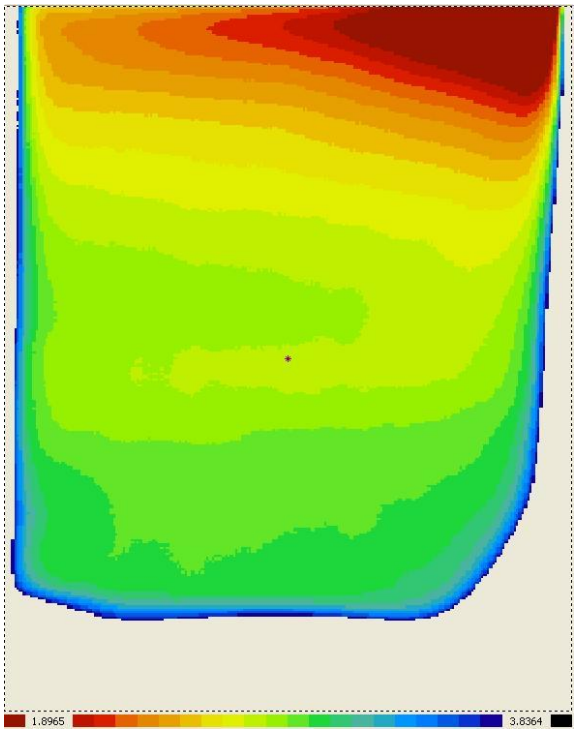

Figure 4.24: Mapping of resistivity in IC5 by eddy currents.

4.4.3 IC6

Figure 4.25 presents the lifetime map of IC6, which was grown in the NBSN crucible. As is shown in the figure, the seeding layer used when producing this ingot was much larger than in those that preceded. Additionally, the red zone appears to be large both in the bottom and near the crucible sidewalls. The blue zone is considerably more diffuse than in ingots IC4 and IC5, both with respect to the boundary separating the blue and red zones, as well as the degree of integrity. Towards the upper region, the blue zone becomes increasingly concave. Defects or impurities do not appear to pervade the blue zone, but some irregularities in the form of sites with lower lifetime are present.

Including the diffuse blue region, IC6 is set apart from the earlier ingots by the fact that the red zone manages to invade the upper boundary of the blue zone. The total lifetime is also lower, as it reaches 6.21 µs in the blue zone.

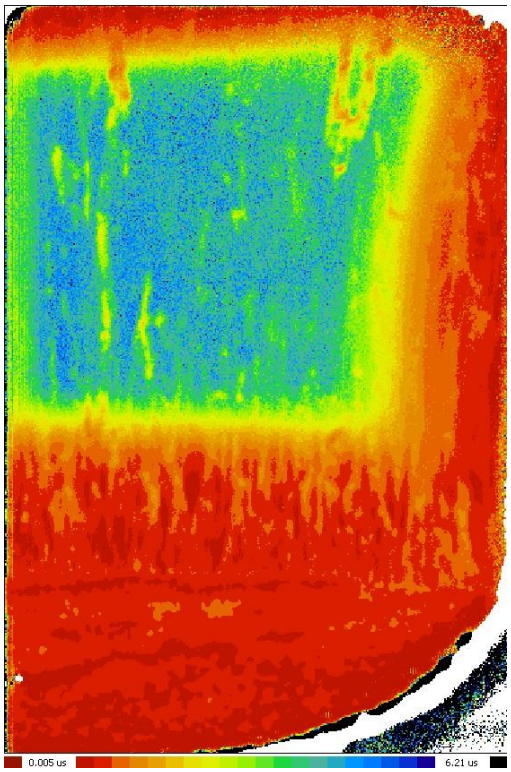

Figure 4.25: Mapping of carrier lifetime in IC6 by µPCD.

The resistivity mapping of IC6, shown in figure 4.26, is not comparable to the preceding ingots. The immediately observable difference from the other ingots thus far is the acute decrease in resistivity after the seeding layer. Additionally, there resistivity gradient that was found in IC4 and IC5 is not present in this ingot to the same extent. Just above the seeding layer, the resistivity remains uniform throughout most of the main body. IC6 also stands apart from the preceding ingots by having a resistivity profile that appears to increase slightly towards the crucible sidewalls.

Due to the lack of a clear gradient, it is hard to discern to what extent the resistivity decreases towards the upper right, as it did for IC4 and IC5. Despite this, the lowest resistivity was measured in this area with a value of 0.24063 Ωcm. High resistivity was almost exclusively confined to the seeding layer, and was maximized at 6.815 Ωcm. The majority of the ingot displayed a resistivity approaching 1 Ωcm, which is in agreement with the measurements performed with FPP.

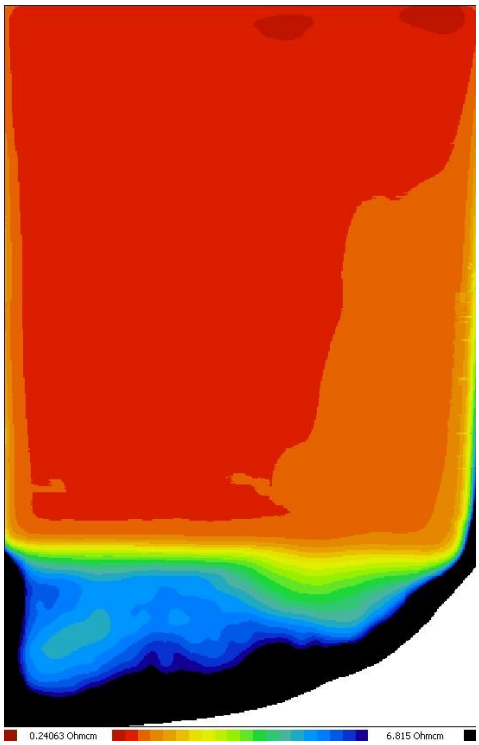

Figure 4.26: Mapping of resistivity in IC6 by eddy currents.

4.4.4 IC7

The carrier lifetime map for IC7 is shown in figure 4.27. The carrier lifetimes and zones are highly irregular compared with earlier results. First of all, the red zone growing from the seeding layer appear to be uneven, deformed and invades into the blue zone from both the bottom and upper part of the ingot. The degree of invasion from above is particularly interesting, as seems to annihilate the blue zone while permeating into the ingot along grain boundaries. Compared to the other ingots, the grain boundaries in IC7 are clearly visible due to the low lifetime at these sites. They are especially visible in the blue zone, which clearly has achieved a concave shape after approximately 50% solidification. Consequently, the red zone also occupies more of the ingot's volume near the crucible sidewalls.

Another interesting feature is the orientation of the grains and how it changes by crucible height. At the lower and upper blue zone, the density of low lifetime sites appears to be particularly high. This is depicted in the blue zone as yellow regions with intermediate lifetimes. In both the upper and lower blue region in IC7, these intermediate lifetimes do not appear at grain boundaries but rather cover entire grains.

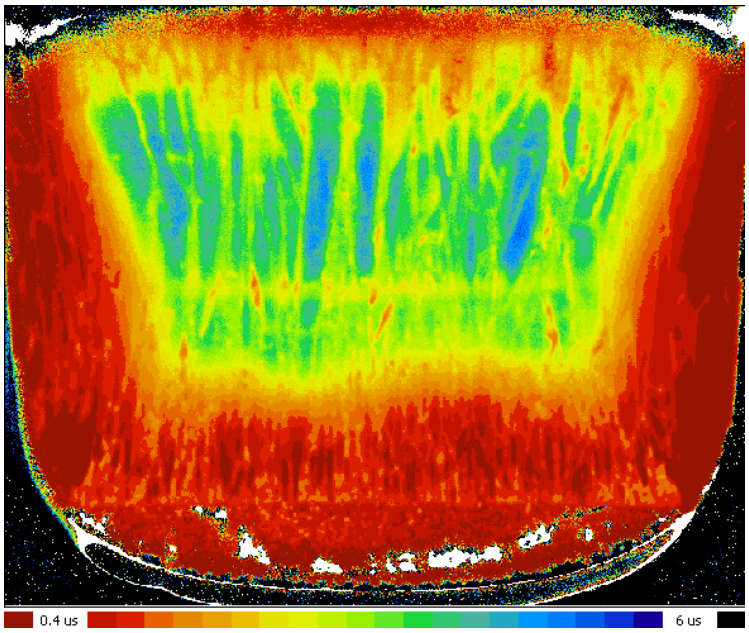

Figure 4.27: Mapping of carrier lifetime in IC7 by µPCD.

The resistivity map for IC7 is shown in figure 4.28. The resistivity distribution is comparable to that of IC5, in the sense that it becomes increasingly lamellar towards the upper surface. Because the sample was analyzed as a complete cross section of IC7, the tendency for low resistivity to be segregated towards the crucible wall during the late solidification stage is now more clearly observed.

Interestingly, the high resistivity associated with the seeding layer appears to be unique in IC7, relative to the previous experiments. The horizontal, slightly concave outline of a seeding layer can be discerned from figure 4.28, but the resistivity in parts of this section is actually comparable to that of the upper ingot. This is represented as a yellow or green hue in the figure.

It should be noted that the black area seen in both figure 4.26 and 4.28 is due to the bounds imposed on the analysis programme. If the upper bounds were set to a higher value, for instance 4 Ωcm in figure 4.28, it would be at the loss of details for the lower bound. Because the primary interest for this thesis is in the ingots as a whole, the resistivity resolution near the seeding layer was sacrificed.

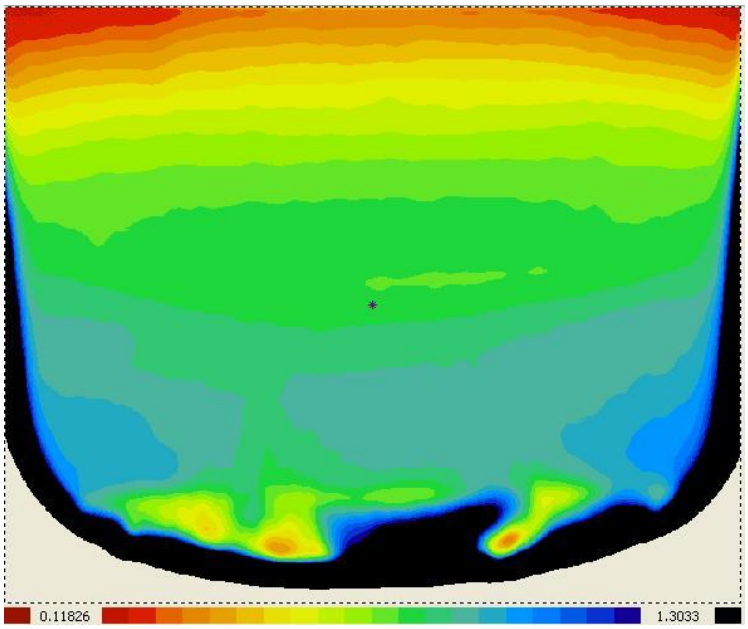

Figure 4.28: Mapping of resistivity in IC7 by eddy currents.

4.5. Scheil plots

This section presents the Scheil plots made for each ingot to qualitatively verify how well resistivity measurements correlate with the Scheil model. The data points presented in each plot are the resistivity measurements obtained by FPP, whereas the pink line in each figure is the Scheil curve for resistivity.

The Scheil curves in this section are regression curves constructed by first using the ingot dimensions to calculate a mass fraction f_M for the silicon load, which is analogous to the solidification fraction f_S. The Scheil model, given by equation 2.14, was then used together with f_M to calculate values for resistivity with respect to boron segregation with $k_0 = 0.78$. By using the least square method and a measured resistivity near the seeding layer as an initial value, the model was fitted and optimized to the measurements. However, in order to obtain a reasonably good fit to the model, it was required to omit some of the resistivity measurements that were taken from the seeding layer. The error bars for each data point were calculated as the sum of squared difference the measurements and the mean.

The yellow line in each plot represents the ingot solidification fraction f_S, starting from the seeding layer.

4.5.1 IC4

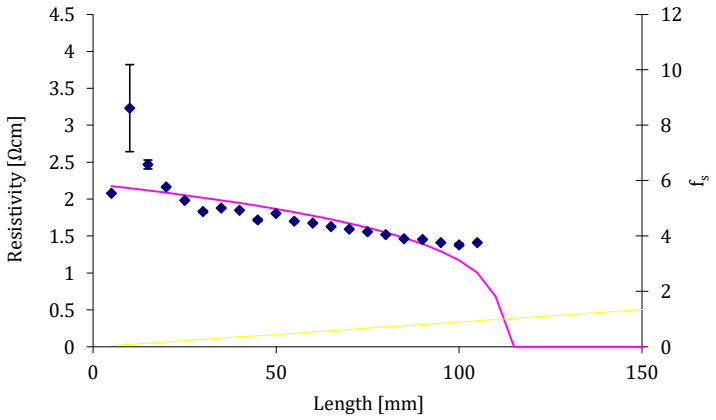

Figure 4.29: Scheil plot with the mean resistivity of IC4. Measurement length was 105 mm.

4.5.2 IC5

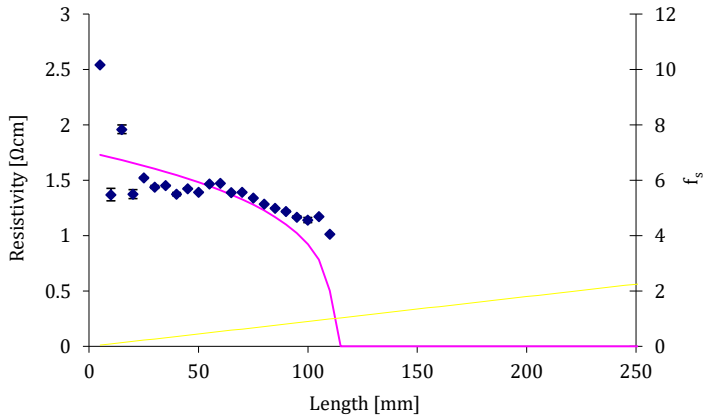

Figure 4.30: Scheil plot with the mean resistivity of IC5. Measurement length was 110 mm.

4.5.3 IC6

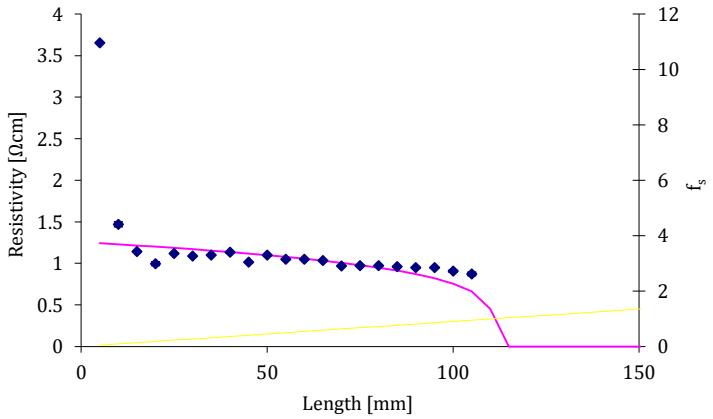

Figure 4.31: Scheil plot with the mean resistivity of IC6. Measurement length was 110 mm.

4.5.4 IC7

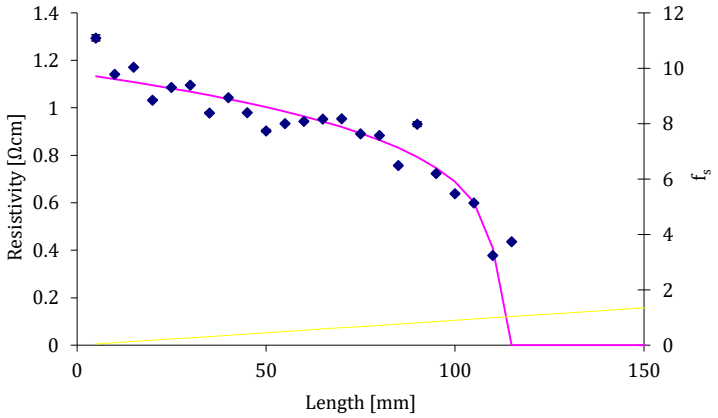

Figure 4.32: Scheil plot with the mean resistivity of IC7. Measurement length was 115 mm.

4.6. Gas chromatography

In situ gas chromatography was performed during the melting and solidification of all ingots. By investigating the relative composition of evaporates from the melt, it was hoped that the extent and knowledge of ingot contamination by dissolving and back-diffusing gasses could be better understood. Gases were measured not as partial pressures, but rather as number of detected molecules at a given time. As is shown in the figures 4.33 to 4.36 in this section, the number of detected molecules does not increase linearly with time but rather oscillates. This oscillation is caused by periodic venting of the furnace.

However, as is shown in figures 4.33 to 4.36, only figure 4.33 represents accurate chromatography of the DS process. The staff responsible for DS growth of ingots IC4-IC7 experienced technical difficulties in using gas chromatography, thus resulting only in satisfactory results for IC4. Although the gas chromatography for IC5 may be concluded to be inaccurate due to the oscillating measurements, it does still provide some insight into the relative amount of present gases.

As can be seen in figure 4.34, the amounts of gases in IC5 resemble those found during gas chromatography of IC4. In both solidification processes, the oxygen partial pressure

increased past the 5000 mark within the first hour of operation, before diminishing to 200 in IC4 and 120 in IC5 after the first venting cycle. CO_2 followed the same trend in both processes by increasing to 2900 within the first hour before eventually being reduced under 100. This reduction took 6 hours for IC4 and less than 30 minutes for IC5. In IC4, the N_2 gas phase steadily increased from 800 to over 1100 throughout the process, even despite adhering to the venting schedule. In IC5, the N_2 gas phase was stable at 500 through the whole process. In both processes, CO appears to be the gas phase most affected by the venting cycle as demonstrated by their undulating chromatography curves. IC4 experienced the most emission of CO, peaking at 2500 after 8 hours of processing, followed by a cyclic decrease to 300 after 42 hours. In comparison, CO emission in IC5 was modest as it peaked at 1000 after 5 hours of processing before decreasing to 300 at end of ingot growth. Due to the unsatisfactory gas chromatography of IC5, the measurements were ended after only 15 hours of solidification.

The gas chromatography of samples IC6 and IC7, shown in figure 4.35 and 4.36, are not comparable. Both figures show that the gas chromatograph detected species that were not present in the preceding solidification processes, such as H_2 and CH_4. The gas chromatography for ingot IC7, shown in figure 4.36, also detected argon gas although it is indented as an undetectable mobile phase for the other species. Consequently, these figures are deemed as erroneous and do not represent the actual gases present in the furnace. In all likelihood the gases that were present during solidification in NBSN crucibles would be identical to those found during solidification in Si_3N_4-coated SiO_2 crucibles, although with a different profile. The gas chromatography profiles for IC6 and IC7 were merely included in this thesis to provide an argument as to why no successful identification of gases was obtained from the respective solidification processes.

4.6.1 IC4

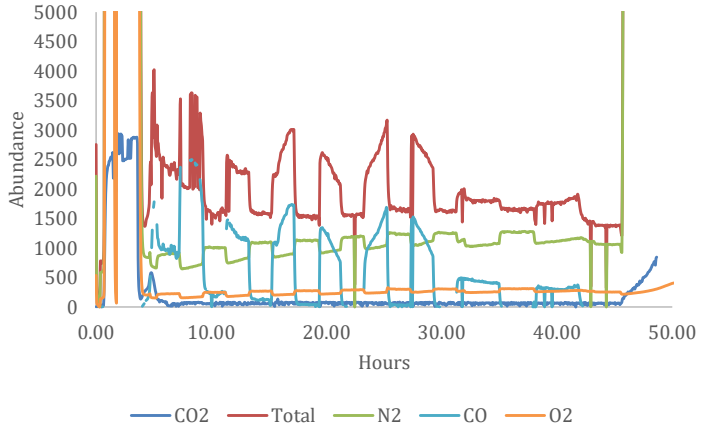

Figure 4.33: *In situ* gas chromatography of IC4.

4.6.2 IC5

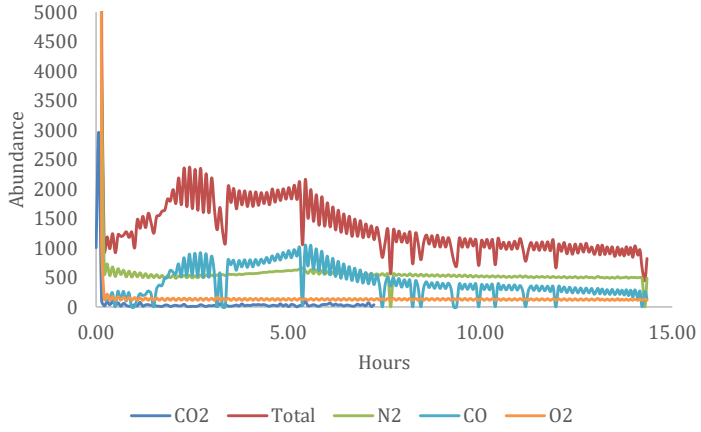

Figure 4.34: *In situ* gas chromatography of IC5.

4.6.3 IC6

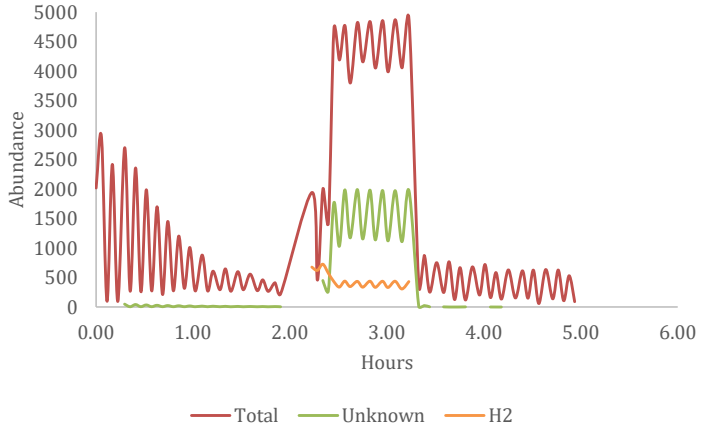

Figure 4.35: *In situ* gas chromatography of IC6.

4.6.4 IC7

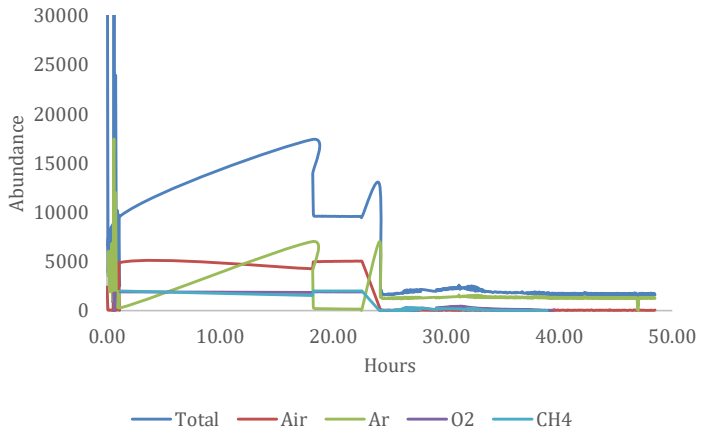

Figure 4.36: *In situ* gas chromatography of IC7.

5. Discussion

5.1. Degree of wetting on oxidized NBSN

Figure 4.1 and 4.3, respectively, show the contour of spherical silicon droplets solidified on uncoated and coated substrates of pre-oxidized NBSN. Although the contact angles are difficult to distinguish with certainty due to the absence of any automated goniometer, it was measured that silicon, in this case, exhibits higher contact angles on the uncoated substrate compared with the coated one. Stated more succinctly: by displaying contact angles between 87^0 and 93^0 on the coated NSBN surface, the coating would appear to exhibit slightly wetting contact with liquid silicon. On the other hand, the uncoated NBSN substrate forms clearly non-wetting contact by achieving 97^0 and $106\ ^0$ angles with silicon. The behaviour seems to contradict the coating's functions which are, as exemplified in a paper by Drevet *et al.*[17], to act as a barrier against crucible wetting and infiltration by silicon, while also acting as a means of detachment between crucible and ingot.

However, Drevet *et al.* also remarked in the same paper that the initial contact angle θ_0 between liquid silicon and an oxidized Si_3N_4 substrate was found to be $\theta_0 = 92^o \pm 3^o$, which decreased to $\theta_C = 45^o \pm 3^o$ after allowing the droplet to spread. This spreading and subsequent decrease in contact angle was attributed to deoxidation of the substrate by formation of $SiO_{(g)}$. Considering how the contact angle in this thesis was stabilized at $\theta_0 = 101{,}5^o \pm 4{,}5^o$ for the uncoated substrate and remained unchanged even from initial silicon melting, this could be an argument against appreciable substrate deoxidation during the directional solidification process. Drevet *et al.* also remarked that the presence of impurities such as carbon, as well as porosity, will act as agents for deoxidation and subsequently contribute to contact angle reduction.

Schneider *et al.*[24], who specifically investigated the wetting action of silicon on oxidized NBSN, reported that the contact angle remained constant on the uncoated substrate if it had been pre-oxidized prior to wetting, as opposed to unoxidized samples where the angle decreased from 120º to 60º over the course of 3 hours. Their reported constant wetting angle would appear to correlate well with the wetting behaviour displayed in this thesis. Moreover, Schneider observed that the measured contact angle increased with substrate oxidation temperature and oxygen content in the atmosphere during preparation. The maximum angle was reported as 149º, which was observed on a substrate oxidized at 1200 ºC and in an

atmosphere of 20,9 vol% O_2. The angular difference between Schneider's results and those presented in this thesis could indicate that pre-oxidation of the uncoated NBSN substrate was either not performed in a sufficiently oxygen-enriched atmosphere, or at sufficiently high temperatures.

By reviewing figure 4.1 and 4.3 with respect to the degree of formation of the film or smear on the substrate, it is confirmed that the coating does reduce adhesion between silicon melt and substrate. The silicon film covering the substrate is considerably reduced for the coated substrate, both in terms how much surface area has been covered by the running liquid and the penetration depth. Admittedly, the latter observation is only confirmed visually by observing the change in coloration and texture, and has not been further investigated by any form of microscopy. This reduction in film penetration and coverage may appear counterintuitive with respect to the observed contact angle in each sample, but could be explained by how Si_3N_4 coating decreases the interface surface energy due to its porosity being much higher than the substrate. This is caused by the submicron grains that form oxidized channels, which prevent capillarity, after having been fused during drying at temperatures[34] such as those in table 3.2. Consequently, both the penetration of silicon into the substrate and pull on the outer liquid layer on the droplet is reduced.

Two curious artefacts raise some concern for the interaction between substrate and silicon. The first anomaly was the observed vibration that occurred during liquefaction of silicon, while the other was the formation of an outgrowth or "hat" on the droplet as it solidified. The exact cause of their existence is unclear, but it is worth noting that they both appear more vividly in the sessile drop situated on the uncoated substrate. The suspected cause to this behaviour was attributed to deoxidation of the oxidized NBSN surface by reaction with silicon, thus creating $SiO_{(g)}$ or $SiO_{2(g)}$ at the interface. This unintentional reaction could potentially explain why the droplet was displaced slightly towards the substrate edge during the course of melting, as shown in figure 4.2, by partially detaching it from the substrate. However, no increase or oscillation in oxygen partial pressure was detected while this displacement occurred.

Regardless whether release of oxygen does plays an important role in the displacement, the fact that both anomalies were observed to appear more vigorously on the uncoated substrate suggests that oxygen remains an important factor for this behaviour. As for the outgrowth during droplet cooling, it is well known that silicon is one of the few materials that expands during solidification. Because the solid silicon cannot force itself through the substrate during expansion, the path of least resistance would be the droplet surface. It is therefore suggested that some dissolved oxygen remains and has failed to evaporate from the droplet surface prior

to solidification. When cooling, the droplet solidifies radially inwards and entraps the dissolved oxygen, thus forcing it upwards. The combined effect of radial solidification, thermal expansion and oxygen evaporation forces the outgrowth to form.

However, it should be clarified that without any means or incentive to study the sessile drop microstructure, this is merely a postulation to the reason for discrepancy between uncoated and coated NBSN substrates.

5.2. Impurity distribution in the ingot

Impurity concentrations and distributions in the ingots were primarily investigated by FTIR with respect to interstitial oxygen and substitutional carbon. Although other impurities such as transition metals were undetectable by FTIR, their presence was qualitatively evaluated by µPCD and eddy current mapping by taking into consideration their segregation coefficient, diffusivity and effect on carrier lifetime. However, the inability to precisely determine the concentration of transition metals and other elements that function as trapping and recombination sites makes their distribution in the ingot more speculative.

5.2.1 Oxygen contamination

One of the greatest motivations for investigation NSBN crucibles as a valid alternative to silica crucibles is due to the adverse effect that oxygen has on ingot conductivity. Although oxygen complexes only reduce mc-Si solar cell efficiency by a few percent, the formation of larger precipitates may induce shunting and structural weakness in the ingot. As mentioned in section 2.2.4, the incorporation of oxygen into the silicon ingot originates at the melt-crucible interface where oxygen either diffuses into the melt or is dissolved by melt that manages to invade past the silicon nitride coating layer. Consequently, oxygen inclusion into the ingot must be reduced as much as possible, either by minimizing its content in the crucible or by preventing dissolution and diffusion reactions.

The interstitial oxygen concentration profiles, which were measured by FTIR and shown in figure 4.19, depict that oxygen is largely confined to the seeding layer during ingot growth. This is especially the case for IC4 and IC5, which were grown in conventional silica crucibles. Interstitial oxygen confinement to the seeding layer is ideal for mc-Si as it is the center body (blue zone) which is extracted and further processed. This confinement effect

exhibited in ingots grown from silica crucibles might be explained by oxygen's segregation coefficient being higher than unity, as shown in table 2.1. Because it exceeds unity, the oxygen profile cannot be accurately predicted by the Scheil model. This causes oxygen to prefer segregation in solid silicon over the liquid phase, thereby allowing it to diffuse into the seeding layer before the entire silicon load has been melted down. As shown in figures 3.1 to 3.4, all ingot temperature profiles display a holding stage before directional solidification is initiated. This would allow oxygen to diffuse further into the seeding layer and accumulate at preferential sites like grain boundaries, of which the seeding layer contains has in dense abundance. Subsequently, the oxygen is largely inhibited from diffusing back into the receding melt phase by the temperature gradient at the growth interface.

As a consequence of this oxygen confinement into the seeding layer and the implemented venting system, it would appear that evaporated oxygen has not diffused back to the ingot through the melt meniscus in an appreciable extent. If this was the case, the oxygen concentration distribution in figure 4.19 would have been less uniform at higher ingot height.

In figure 4.19, the ingots IC6 and IC7, which were both grown in NBSN crucibles, display a markedly different concentration profile from their predecessors. Especially IC6 is distinguished by its oxygen distribution, which suggests that a confinement effect towards the seeding layer was not present during ingot growth in NBSN crucibles. This could possibly be explained by the fact that temperature profiles for IC6 and IC7, shown in figures 3.3 and 3.4, do not include an annealing stage after solidification. Annealing stages are holding stages at high temperatures, commonly used to reduce defects and dislocation in solids, thus reducing the number of preferential impurity sites as an added benefit. However, annealing at high temperatures just after solidification could possibly cause the seeding layer to contaminate the ingot further by internal diffusion, rather than forcing oxygen transport towards the seeding layer.

Another explanation to the less confined oxygen profile in figure 4.19 would have been that ingot IC6 was grown too quickly, thus oxygen would not have been allowed sufficient time to diffuse into the seeding layer. This explanation would have made sense, but a quick review of figures 3.1 to 3.4 indicates that the temperature change near the seeding layer during solidification is comparable for all ingots.

The interstitial oxygen concentration for IC7 may provide a clue as to why oxygen in IC6 is so different from IC4 and IC5. First of all, recall that IC7 was grown in the NBSN crucible reused from IC6. As shown in figure 4.19, its concentration profile resembles the ones from IC4 and IC5. Judging by its concentration drop at an ingot height comparable to those of

IC4 and IC5, it even exhibits an oxygen confinement to the seeding layer. In addition, by considering the area under each concentration curve, it appears that the total amount of oxygen in IC7 is considerably lower than in IC6. Based on these considerations, the change in oxygen concentration profile and oxygen content suggests that IC6 was supersaturated by oxygen, even after melting the entire silicon load. As ingot growth was initiated, the saturation level was reduced and oxygen could segregate into the growing ingot.

Because it is well known that the crucible is the primary source of oxygen contaminants during melt formation, as explained in section 2.2.4, this high level of oxygen contamination in the first ingot suggests that the silicon melt actively invades past the silicon nitride coating and reaches the crucible. The invading melt proceeds to dissolve the outer protective oxide layer of the NBSN crucible's porous channels, before transporting the oxygen back to the melt by natural convection. Following this oxide dissolution is a reaction pathway for evaporating oxygen, as detailed in section 2.2.4 via equations 2.16 to 2.18. Because less oxygen is readily available in the next ingot solidification, the oxygen contamination decreases in IC7.

The interesting question to ask is perhaps not why the oxygen contamination occurs in IC6 despite using a NBSN crucible in lieu of a conventional silica crucible, but rather why the contamination is so much higher compared to IC4 and IC5.

5.2.2 Carbon contamination

The ingot contamination by substitutional carbon is shown in figure 4.20. As compared to oxygen and given in table 2.1, carbon has a much smaller segregation coefficient and is therefore expected to behave more in accordance with the Scheil model. This means that carbon distribution in silicon should follow figure 2.18, that is to say increase with ingot height. As mentioned in section 4.2.2, the carbon concentrations appear to adhere reasonably well with the model. However, the ingots IC6 and IC7 are again distinguished from IC4 and IC5 by displaying exceedingly high carbon content. For instance, IC4 only experiences a modest concentration increase from approximately 1,5 ppma to 12 ppma from seeding layer to ingot top, whereas IC6 increases from 6,4 ppma to 21,4 over the same length. However, both cases are still above the 7 ppma carbon limit that is imposed on conventional silicon solar cells.

This increased carbon concentration in ingots solidified in NBSN crucibles is likely caused by the co-dependence that carbon manifests with oxygen during ingot growth. By yet again consulting section 2.2.4 and the governing gas flow reactions present in the furnace, it would appear that carbon incorporation is directly proportional to evaporation rate of oxygen

from the melt surface. Because the oxygen supersaturation in IC6 causes more oxygen to evaporate and react with carbon from the heating element, more CO would likely have the opportunity to dissolve into the melt before being evacuated by the venting system. Interestingly, the carbon concentration and distribution in IC7 appears to be comparable with the ones measured in IC6, even when considering that the oxygen content in IC7 is less and should indicate less oxygen evaporation.

5.2.3 Carrier lifetimes and ingot resistivity

Carrier lifetime maps in section 4.4, which were collected by µPCD, show clear differences between reference ingots cast in silica crucibles and the experimental ingots cast in NBSN crucibles.

As the grains grow from the seeding layer, any notable grain boundary mismatch between adjacent grains will cause strain and ultimately dislocations as they collide. Carrier lifetimes are reduced considerably at collision points, either as a result of the dislocations themselves acting as recombination sites or in conjunction with impurities, possibly in the form of precipitates.

Fortunately, both IC4 and IC5 were nearly identical with respect to definition and shape of the high-lifetime region, as well as in terms of maximum measured carrier lifetime. The regularity of both the surrounding red zone and lack of low-lifetime artifacts inside the high-lifetime region are indicative of a low mechanical strain on the ingots as a whole. As seen in both figures 4.21 and 4.23, no grain boundary inclined towards the ingot center can be seen in the red zone parallel to the crucible sidewall. This absence of notable thermal strain owes to the joined thermal expansion between ingot and the silica crucible. It is well known in the mc-Si solar cell industry that silicon expands when undergoing a phase transition from liquid to solid. Consequently, if the surrounding crucible has a comparable thermal expansion, the dislocation generation can be greatly reduced. In this respect silica is well suited for ingot growth, but the expansion does cause crucible fracture which inhibits subsequent use.

The mismatch between thermal expansion in silicon and NBSN is the most likely reason for thermal strain in IC6 and IC7. Silicon nitrides are mechanically rigid and less expansive with increased temperature, thus imposing strain on solidifying silicon.

Additionally, the higher thermal conductivity could possibly explain the orientation and size of the red zone along the NBSN crucible sidewall. Figure 4.27 implies that silicon was nucleation on the crucible sidewall already in the initial stages of solidification. As directional

solidification is caused by a vertical temperature gradient, this inclined nucleation at the sidewall could possibly mean that the main cause for grain mismatch and thermal strain is the growing ingot is a horizontal heat leak through the sidewall.

Another feature worth remarking is the low lifetimes shown in the upper region in figure Figure 4.27, colored red. These are likely dissolved carbon that invades the center ingot.

6. Conclusion

In comparison with the reference ingots solidified with silica crucibles, the mc-Si ingots directionally solidified in NBSN crucibles display elevated concentrations of both oxygen and carbon, particularly in the seeding layer. While oxygen concentrations were below the standard values of 5-10 ppma in all sample ingots, the carbon distribution in both IC6 and IC7 exceed the 7 ppma limit at approximately 50% solidification.

In terms of purity with respect to oxygen, the ingot contamination was reduced to the point of being comparable with conventionally cast ingots after only one NBSN crucible reuse. However, only a marginal reduction in carbon content was detected in IC7, which could possibly be linked to an alternative contaminant reaction pathway involving SiC formation. Furthermore, as shown by eddy current measurements, the decrease in resistivity was concentrated towards the crucible sidewall at higher solidification. This suggest that mobile species, such as boron and carbon, are accumulated towards the crucible sidewall by melt convection. This distribution of impurities by melt convection would agree with the gradual reduction of Marangoni vortices, as discussed in section 2.2.7.

The reduction in oxygen contamination between reuse of NBSN crucibles is considered attributable to the dissolution of available oxide covering NBSN pore structures. As only two NBSN ingots were produced and investigated, it is uncertain what the ramification of this oxide dissolution will have on crucible reusability. However, the extent of non-wetting contact and stability has been confirmed in other research as displaying a certain proportionality with oxidation of internal pores.

The main detriment in reusing the NBSN crucible appears to be the increased thermal strain imposed on the ingot, which generates dislocations. In order for NBSN crucibles to be commercially feasible, it is imperative to reduce horizontal heat leak through the crucible sidewall while improving melt convection. The distorted high-lifetime region in IC6 and IC7, as shown in section 4.2.5 and 4.2.6, are possibly induced by a slightly concave ingot solidification front caused by strong melt convection and high solidification rate.

7. Further work

The primary aim of this thesis was to investigate the possibility of reusing a NBSN crucible and how the reused crucible affects ingot properties with respect to carrier lifetime, resistivity and impurity content. It was discovered that reuse of NBSN crucibles is feasible, as impurity content of O_i reduces and the integrity of the crucible is preserved. However, the C_s reduction in a new ingot was marginal and the suspected dissolution of oxide covering the crucible microstructure was attributed to the increased thermal strain that was observed in IC7 by µPCD. Unfortunately, no conclusive data could be extracted from *in situ* gas chromatography due to technical difficulties.

At the time of concluding this thesis, the Ecosolar project has managed to successfully growth IC9 in the same NBSN-crucible used in this work. In other words, the reusability of a single NBSN crucible has been confirmed for at least 3 consecutive solidifications. Ideally, further work should seek to reduce horizontal heat leak during solidification as this caused considerable thermal strain in ingot IC7. This could possibly be done by altering the crucible composition by increasing SO_2 content, thus preferably creating an amalgamated crucible that exhibits sufficient structural integrity to allow reuse, while at the same time attaining a thermal expansion coefficient and thermal conductivity that approaches silica.

Further research might also want to consider how silicon microstructure changes with NBSN crucible reuse, either through investigation by electron microscope or infrared transmission microscope. The latter would provide insight in the distribution of and density of silicon nitride fibers in the ingot.

8. Bibliography

1. Yang Y, Yu A, Hsu B, Hsu W, Yang A, Lan C. Development of high-performance multicrystalline silicon for photovoltaic industry. Progress in Photovoltaics: Research and Applications. 2015;23(3):340-51.
2. Green MA, Emery K, Hishikawa Y, Warta W, Dunlop ED. Solar cell efficiency tables (Version 45). Progress in photovoltaics: research and applications. 2015;23(1):1-9.
3. Cuevas A, Kerr MJ, Samundsett C, Ferrazza F, Coletti G. Millisecond minority carrier lifetimes in n-type multicrystalline silicon. Applied Physics Letters. 2002;81(26):4952-4.
4. Atkins PW, Friedman RS. Molecular quantum mechanics: Oxford university press; 2011.
5. Streetman BG, Banerjee S. Solid state electronic devices: Prentice Hall New Jersey; 2015.
6. McEvoy A, Castaner L, Markvart T. Solar cells: materials, manufacture and operation: Academic Press; 2012.
7. Søndenå R, Søiland A-K, Angelskår H, Holt A. Light induced degradation in mc-Si based on compensated silicon. Energy Procedia. 2012;27:70-5.
8. Kayamori Y, Dhamrin M, Hashigami H, Saitoh T, editors. Rapid initial light-induced degradation of multicrystalline silicon solar cells. Photovoltaic Energy Conversion, 2003 Proceedings of 3rd World Conference on; 2003: IEEE.
9. Autruffe A, Vines L, Arnberg L, Di Sabatino M. Coincident site lattice bi-crystals growth—Impurity segregation towards grain boundaries. Journal of Crystal Growth. 2015;416:8-11.
10. Callister WD, Rethwisch DG. Materials science and engineering: an introduction: Wiley New York; 2007. 92-107 p.
11. Lan C-w, Hsu C, Nakajima K. Multicrystalline Silicon Crystal Growth for Photovoltaic Applications. Handbook of Crystal Growth: Bulk Crystal Growth. 2015:373-411.
12. Scheel HJ, Capper P, Rudolph P. Crystal Growth Technology: Semiconductors and Dielectrics: John Wiley & Sons; 2011.
13. Li TF, Huang HC, Tsai HW, Lan A, Chuck C, Lan CW. An enhanced cooling design in directional solidification for high quality multi-crystalline solar silicon. Journal of Crystal Growth. 2012;340(1):202-8.
14. Li JG, Hausner H. Wetting and adhesion in liquid silicon/ceramic systems. Material Letters. 1992(14):329-32.
15. Dr. Bert Geyer, Gerd Schwichtenberg, Miiller DA. Increased wafer yield in silicon ingots by the application of high purity silicon nitride coating and high purity crucibles. IEEE Journal of Photovoltaics. 2005:1059 - 61.
16. Li JG. Wetting of Ceramic Materials by Liquid Silicon, Aluminium and Metallic Melts Containing Titanium and Other Reactive Elements: A Review. Ceramics International. 1994;20:391-412.

17. Drevet B, Pajani O, Eustathopoulos N. Wetting, infiltration and sticking phenomena in Si3N4 releasing coatings in the growth of photovoltaic silicon. Solar Energy Materials and Solar Cells. 2010;94(3):425-31.
18. Bellmann MP, Meese EA, Syvertsen M, Solheim A, Sørheim H, Arnberg L. Silica versus silicon nitride crucible: Influence of thermophysical properties on the solidification of multi-crystalline silicon by Bridgman technique. Journal of Crystal Growth. 2011;318(1):265-8.
19. Richard J. Phillips, Steven L. Kimbel, Aditya J. Deshpande, Shi G. Coating compositions. United states patent. 2012.
20. Chandra P. Khattak D, Schmid F. Reusable crucible for silicon ingot growth. United states patent. 2004.
21. Rune Roligheten, Gjertrud Rian, Julsrud S. Reusable crucibles and method of manufacturing them. United states patent. 2009.
22. Zhao L, Lv T, Zhu Q. Si3N4/fused quartz composite crucible with enhanced thermal conductivity for multicrystalline silicon ingot growth. Journal of Crystal Growth. 2015;415:51-6.
23. Schneider V, Reimann C, Friedrich J, Müller G. Nitride bonded silicon nitride as a reusable crucible material for directional solidification of silicon. Crystal Research and Technology. 2016;51(1):74-86.
24. Schneider V, Reimann C, Friedrich J. Wetting and infiltration of nitride bonded silicon nitride by liquid silicon. Journal of Crystal Growth. 2016;440:31-7.
25. Morita K, Miki T. Thermodynamics of solar-grade-silicon refining. Intermetallics. 2003;11(11-12):1111-7.
26. Bellmann MP, Meese EA, Arnberg L. Impurity segregation in directional solidified multi-crystalline silicon. Journal of Crystal Growth. 2010;312(21):3091-5.
27. Macdonald D, Cuevas As, Kinomura A, Nakano Y, Geerligs LJ. Transition-metal profiles in a multicrystalline silicon ingot. Journal of Applied Physics. 2005;97(3):033523.
28. Gao B, Chen XJ, Nakano S, Kakimoto K. Crystal growth of high-purity multicrystalline silicon using a unidirectional solidification furnace for solar cells. Journal of Crystal Growth. 2010;312(9):1572-6.
29. Raabe L, Pätzold O, Kupka I, Ehrig J, Würzner S, Stelter M. The effect of graphite components and crucible coating on the behaviour of carbon and oxygen in multicrystalline silicon. Journal of Crystal Growth. 2011;318(1):234-8.
30. Trempa M, Reimann C, Friedrich J, Müller G. The influence of growth rate on the formation and avoidance of C and N related precipitates during directional solidification of multi crystalline silicon. Journal of Crystal Growth. 2010;312(9):1517-24.
31. Arafune K, Ohishi E, Sai H, Ohshita Y, Yamaguchi M. Directional solidification of polycrystalline silicon ingots by successive relaxation of supercooling method. Journal of Crystal Growth. 2007;308(1):5-9.
32. Nakano S, Gao B, Kakimoto K. Relationship between oxygen impurity distribution in multicrystalline solar cell silicon and the use of top and side heaters during manufacture. Journal of Crystal Growth. 2013;375:62-6.
33. G. L. Miller, D. A. H. Robinson, Wiley JD. Contactless measurement of semiconductor conductivity by radio frequency-free-carrier power absorption. Review of Scientific Instruments. 1976;47(7).

34. Selzer A, Brizé V, Voytovych R, Drevet B, Camel D, Eustathopoulos N. Chemical stability of silicon nitride coatings used in the crystallization of photovoltaic silicon ingots. Part I: Stability in vacuum. Journal of the European Ceramic Society. 2016.